Cancer Cell

Article

STAG2 loss rewires oncogenic and developmental programs to promote metastasis in Ewing sarcoma

Graphical abstract

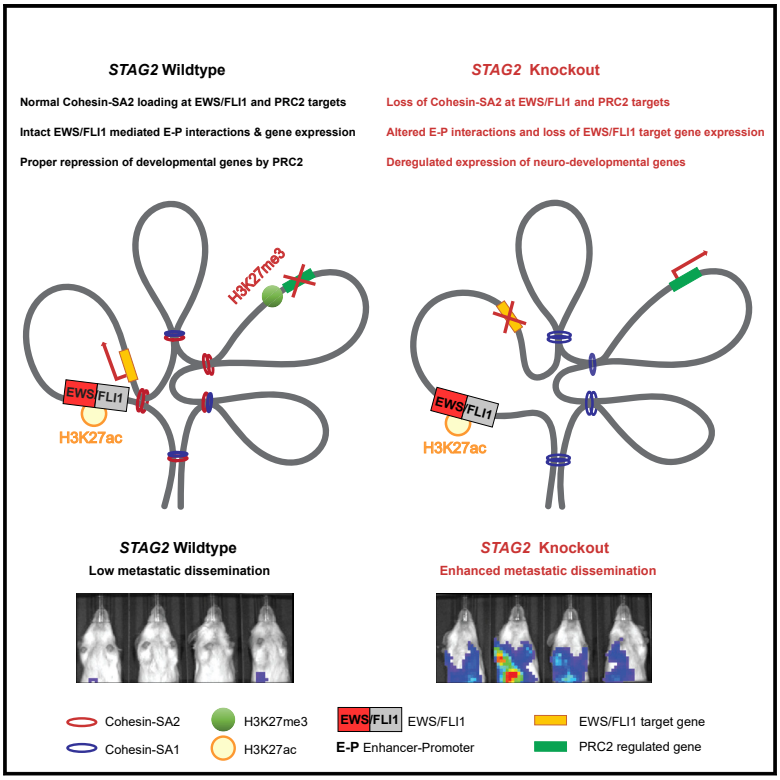

Highlights

- Cohesin-SA2 occupies enhancer and PRC2-marked regulatory regions in Ewing sarcoma
- STAG2 depletion alters a subset of EWS/FLI1 anchored enhancer-promoter interactions
- Loss of STAG2 modifies oncogenic and developmental transcriptional programs
- STAG2 loss enhances the migratory and metastatic potential of Ewing sarcoma cells

Authors

Biniam Adane, Gabriela Alexe, Bo Kyung A. Seong, ..., Richard A. Young, Brian D. Crompton, Kimberly Stegmaier

Correspondence

briand_crompton@dfci.harvard.edu (B.D.C.), kimberly_stegmaier@dfci.harvard.edu (K.S.)

In brief

Adane et al. demonstrate that deletion of STAG2 changes the distribution of cohesin complexes and leads to reprograming of *cis*-chromatin interactions in Ewing sarcoma. STAG2 loss attenuated EWS/FLI1-driven oncogenic programs and disrupted PRC2-regulated developmental processes to enhance the metastatic potential of Ewing sarcoma cells.

Adane et al., 2021, Cancer Cell *39*, 827–844
June 14, 2021
https://doi.org/10.1016/j.ccell.2021.05.007

CellPress

Cancer Cell

CellPress

Article

STAG2 loss rewires oncogenic and developmental programs to promote metastasis in Ewing sarcoma

Biniam Adane,[1,2,12] Gabriela Alexe,[1,2,3,12] Bo Kyung A. Seong,[1,2] Diana Lu,[1] Elizabeth E. Hwang,[1] Denes Hnisz,[4] Caleb A. Lareau,[5] Linda Ross,[1] Shan Lin,[1] Filemon S. Dela Cruz,[7] Melissa Richardson,[8] Abraham S. Weintraub,[4,9] Sarah Wang,[1] Amanda Balboni Iniguez,[1] Neekesh V. Dharia,[1,2] Amy Saur Conway,[1] Amanda L. Robichaud,[1] Benjamin Tanenbaum,[2] John M. Krill-Burger,[2] Francisca Vazquez,[2] Monica Schenone,[2] Jason N. Berman,[10,11] Andrew L. Kung,[7] Steven A. Carr,[2] Martin J. Aryee,[2,6] Richard A. Young,[4,9] Brian D. Crompton,[1,2,*] and Kimberly Stegmaier[1,2,13,*]

[1]Dana-Farber/Boston Children's Cancer and Blood Disorders Center, Boston, MA, USA
[2]Broad Institute of MIT and Harvard, Cambridge, MA, USA
[3]Bioinformatics Graduate Program, Boston University, Boston, MA, USA
[4]Whitehead Institute for Biomedical Research, Cambridge, MA, USA
[5]Department of Pathology, Stanford University, Stanford, CA, USA
[6]Department of Pathology, Massachusetts General Hospital, Charlestown, MA, USA
[7]Department of Pediatrics, Memorial Sloan Kettering Cancer Center, New York, NY, USA
[8]Department of Pathology, Dalhousie University, Halifax, NS, Canada
[9]Department of Biology, Massachusetts Institute of Technology, Cambridge, MA, USA
[10]Department of Pediatrics and Cellular and Molecular Medicine, University of Ottawa, Ottawa, ON, Canada
[11]Children's Hospital of Eastern Ontario Research Institute, Ottawa, ON, Canada
[12]These authors contributed equally
[13]Lead contact
*Correspondence: briand_crompton@dfci.harvard.edu (B.D.C.), kimberly_stegmaier@dfci.harvard.edu (K.S.)
https://doi.org/10.1016/j.ccell.2021.05.007

SUMMARY

The core cohesin subunit *STAG2* is recurrently mutated in Ewing sarcoma but its biological role is less clear. Here, we demonstrate that cohesin complexes containing STAG2 occupy enhancer and polycomb repressive complex (PRC2)-marked regulatory regions. Genetic suppression of STAG2 leads to a compensatory increase in cohesin-STAG1 complexes, but not in enhancer-rich regions, and results in reprogramming of *cis*-chromatin interactions. Strikingly, in *STAG2* knockout cells the oncogenic genetic program driven by the fusion transcription factor EWS/FLI1 was highly perturbed, in part due to altered enhancer-promoter contacts. Moreover, loss of STAG2 also disrupted PRC2-mediated regulation of gene expression. Combined, these transcriptional changes converged to modulate EWS/FLI1, migratory, and neurodevelopmental programs. Finally, consistent with clinical observations, functional studies revealed that loss of STAG2 enhances the metastatic potential of Ewing sarcoma xenografts. Our findings demonstrate that *STAG2* mutations can alter chromatin architecture and transcriptional programs to promote an aggressive cancer phenotype.

INTRODUCTION

Massively parallel sequencing efforts have revealed cancer-associated mutations in the cohesin complex, a multiprotein complex important in sister chromatid cohesion and gene regulation (Romero-Perez et al., 2019). STAG2 is a member of the cohesin complex, composed of SMC1A, SMC3, and RAD21, forming a ringed structure that can surround two strands of DNA. The fourth member of the complex is one of three members of the STAG protein family: STAG1, STAG2, or STAG3 (Haering et al., 2008; Nasmyth, 2002). Studies have demonstrated that cohesin complexes containing either STAG1 (cohesin-SA1) or STAG2 (cohesin-SA2) are expressed concurrently in mitotic cells and bind to overlapping, as well as unique, chromatin locations (Cuadrado et al., 2019; Kojic et al., 2018; Losada et al., 2000). The cohesin complex plays an important role in regulating sister chromatid alignment during cell division. Therefore, when loss-of-function mutations in *STAG2* were first identified in cancer, it was hypothesized that these events would cause cohesin dysfunction and improper chromosomal segregation resulting in aneuploidy (Solomon et al., 2011). However, subsequent studies demonstrated that *STAG2* mutations are not significantly associated with aneuploidy in hematopoietic malignancies, Ewing sarcoma, or bladder carcinoma (Balbas-Martinez et al., 2013; Crompton et al., 2014; Kon et al., 2013; Solomon et al., 2013; Tirode et al., 2014). The cohesin complex also plays a critical role in chromatin regulation of gene expression. Cohesin maintains chromatin accessibility at transcription factor binding sites

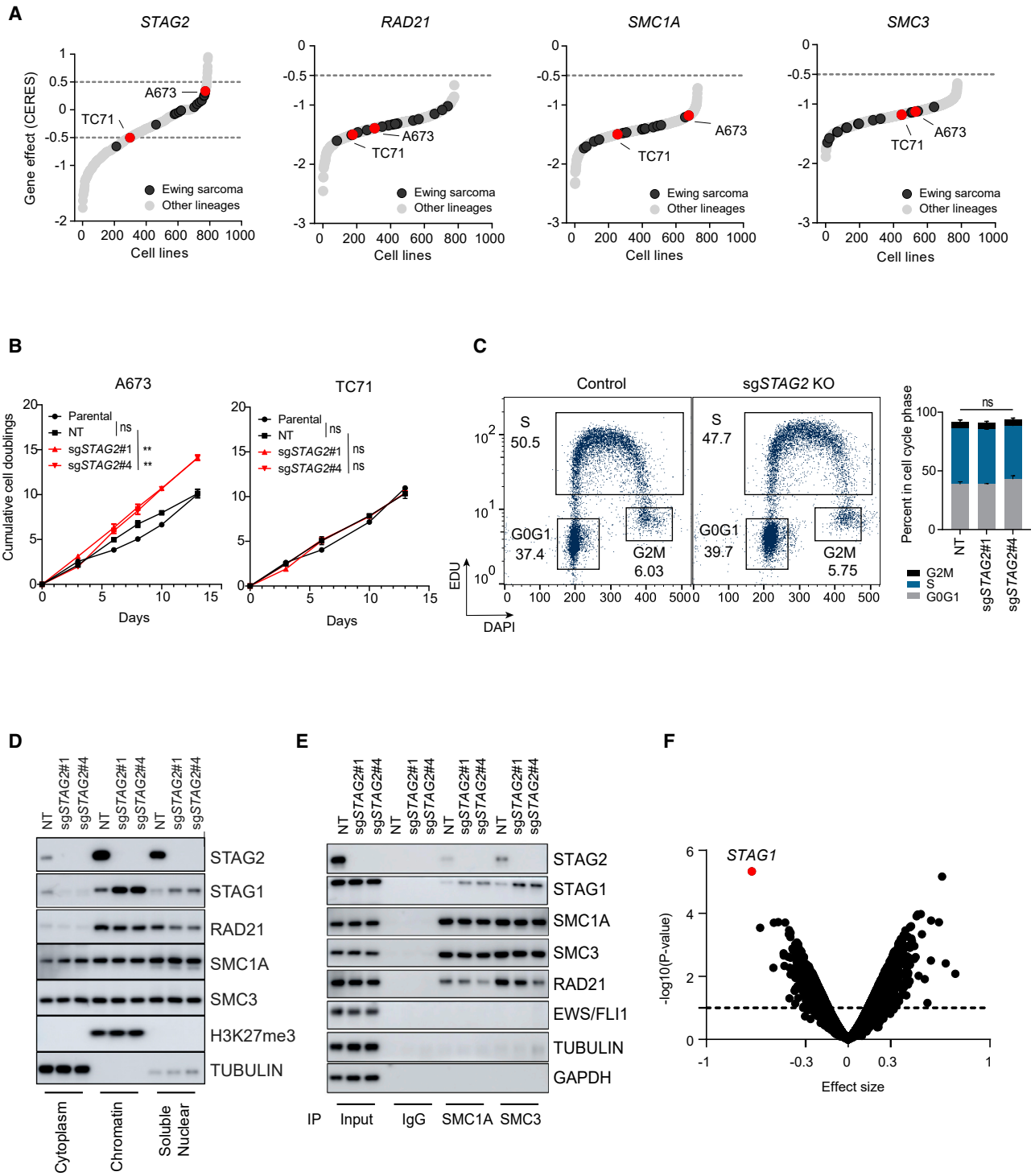

Figure 1. Loss of *STAG2* does not consistently alter cell growth but changes the composition of the cohesin complex and renders cells sensitive to *STAG1* deletion

(A) Hockey plots depicting the distribution of *STAG2*, *SMC1A*, *SMC3*, and *RAD21* gene effect (CERES) scores across the 789 cell lines in CRISPR (Avana) Depmap v20Q3 data.

(B) Line graphs showing mean ± SD of cumulative doublings for parental or clonally selected non-targeting (NT) or *STAG2* KO A673 and TC71 cells. Pairwise comparative analysis for exponential growth fitted curves. Extra-sum-of-squares F test, $^{**}p < 0.01$; ns, not significant.

(C) EdU (5-ethynyl-2′-deoxyuridine) incorporation-based cell-cycle profiling and representative flow-cytometry plots (left) are shown. Two independent experiments as mean ± SD bar plots (right). Two-way ANOVA; ns, not significant.

(D and E) Subcellular fractionation (D) or immunoprecipitation with SMC1A, SMC3, or IgG (E) followed by western blot was performed for the indicated proteins.

(legend continued on next page)

during cell division and promotes DNA-DNA contacts that form the basis of enhancer-promoter interactions and define the boundaries of topologically associated domains at CTCF binding sites (Dowen et al., 2014; Kagey et al., 2010; Wendt et al., 2008). Therefore, we hypothesized that loss of STAG2 alters cohesin function, resulting in changes in gene regulation in Ewing sarcoma.

Studies have demonstrated that patients with *STAG2*-mutated Ewing sarcoma have a higher rate of metastatic disease and worse outcomes (Crompton et al., 2014; Tirode et al., 2014). Therefore, we also hypothesized that altered gene expression associated with STAG2 loss would be associated with an increase in metastatic potential. To test these hypotheses, we chose the pediatric solid tumor Ewing sarcoma as our model system, a malignancy defined by a simple genome and an oncogenic rearrangement between the *EWSR1* gene and an ETS-family transcription factor encoding gene, most commonly *FLI1*, resulting in an EWS/FLI1 fusion. *STAG2* mutations are present in 15%–20% of tumors and lead to loss of expression of the gene (Brohl et al., 2014; Crompton et al., 2014; Tirode et al., 2014). In this study, we genetically ablated *STAG2* in Ewing sarcoma cell lines expressing wild-type (WT) *STAG2* and examined the phenotypic, transcriptional, and epigenetic effects of STAG2 loss.

RESULTS

Depletion of STAG2 alters the composition of the cohesin complex and is synthetic lethal with STAG1 loss

To evaluate the oncogenic role of loss-of-function mutations in *STAG2*, we initially explored the Cancer Dependency Map (DepMap) database (Tsherniak et al., 2017). Our analysis revealed that, distinct from other core subunits of the cohesin complex, CRISPR/Cas9-based disruption of *STAG2* does not affect the proliferation and/or viability of most Ewing sarcoma cell lines (Figure 1A). A subset of cell lines in the database bear *STAG2* mutations. Thus, we focused on two cell lines, TC71 and A673, which express WT *STAG2*. These cell lines, however, show relatively contrasting phenotypes with respect to *STAG2* deletion, with TC71 showing a modest growth defect and A673 showing a modest growth advantage. *STAG2* is an X-linked gene, and our previous study has shown that recurrent mutations of *STAG2* in Ewing sarcoma invariably result in lack of expression of the protein product (Crompton et al., 2014). Thus, we generated isogenic clonal *STAG2* knockout (KO) cells, along with controls, and subjected them to long-term *in vitro* proliferation assays (Figure S1A). In liquid culture, *STAG2*-deleted A673 cells showed a mild, yet statistically significant, growth advantage, consistent with DepMap data (Figure 1B). In contrast, TC71 cells displayed a similar rate of growth relative to non-targeting and parental controls in liquid culture and a mild growth defect in semi-solid methylcellulose media (Figures 1B and S1B). Moreover, given the important role of the cohesin complex in maintaining proper cohesion and segregation of sister chromatids, we also evaluated cell-cycle progression. Our results showed relatively similar distribution of cells in all phases of the cell cycle in control and *STAG2*-deleted A673 cells (Figure 1C).

Because STAG2 is one of the core subunits of the cohesin complex, we next employed biochemical assays and investigated the impact of STAG2 loss on the complex. Purified cytoplasmic, soluble nuclear, and chromatin-bound fractions from control and *STAG2* KO cells were immunoblotted for several cohesin complex subunits. Strikingly, we observed increases in STAG1 levels with *STAG2* KO in the chromatin-bound fraction in A673 and soluble nuclear fraction of A673 and TC71 cells (Figures 1D and S1C). In addition, RAD21 levels were reduced in the soluble nuclear fraction. Next, to test whether changes in STAG2 abundance affect the assembly of the complex, we immunoprecipitated cell extracts with antibodies against SMC1A or SMC3 and immunoblotted for all the core subunits of the complex. Consistent with the cell-fractionation experiments, we observed increased levels of STAG1 and decreased levels of RAD21 in association with the SMC proteins in *STAG2* KO cells (Figures 1E and S1D).

The absence of consistent cell-proliferation alterations, and the increased levels of cohesin-SA1, suggest that at least the essential, cell-cycle-associated function of STAG2 is being compensated by its paralog STAG1. Consistent with this notion and in good agreement with previous findings by other investigators (Benedetti et al., 2017; Liu et al., 2018; van der Lelij et al., 2017), a genome-scale CRISPR/Cas9 screen identified *STAG1* as the top synthetic lethal dependency in isogenic *STAG2* KO A673 cells compared with controls (Figure 1F). This finding was also validated in independent experiments comparing the effect of *STAG1* deletion in isogenic settings, as well as in WT and *STAG2* mutant parental Ewing sarcoma cell lines (Figures S1E–S1H). Taken together, these results strongly suggest that *STAG2* mutations in Ewing sarcoma do not predominantly and universally perturb the canonical cell-cycle-associated function of the cohesin complex and that the likely contribution of these mutations to Ewing sarcoma pathogenesis is through other mechanisms.

Cohesin-SA1 and cohesin-SA2 bind to overlapping and unique regions in Ewing sarcoma cells

In addition to the canonical role of maintaining sister chromatid cohesion during cell division, the cohesin complex also mediates dynamic, high-frequency intrachromosomal interactions including those conjoining enhancers to promoters (Hansen et al., 2018). Therefore, we hypothesized that loss of STAG2 disrupts *cis*-chromatin interactions in Ewing sarcoma cells. First, to determine the genome-wide distribution and relative abundance of the cohesin complexes in the presence and absence of STAG2, we performed calibrated chromatin immunoprecipitation sequencing (ChIP-seq) analysis using antibodies against STAG2, STAG1, and SMC1A in isogenic A673 cells. Consistent with our biochemical analyses, genome-wide binding of STAG1 increased significantly in *STAG2* KO cells (Figures 2A

(F) Genome-scale CRISPR/Cas9 screen in isogenic NT and *STAG2* KO A673 clonal cells. Shown is the volcano plot for gene effect size versus $-\log_{10}$(p value) for the genome-wide differential analysis of isogenic NT versus *STAG2* KO processed reads; dots represent genes (limma eBayes for MAGeCK gene effect scores, effect size ≤ -0.3, adjusted p ≤ 0.10).
See also Figure S1.

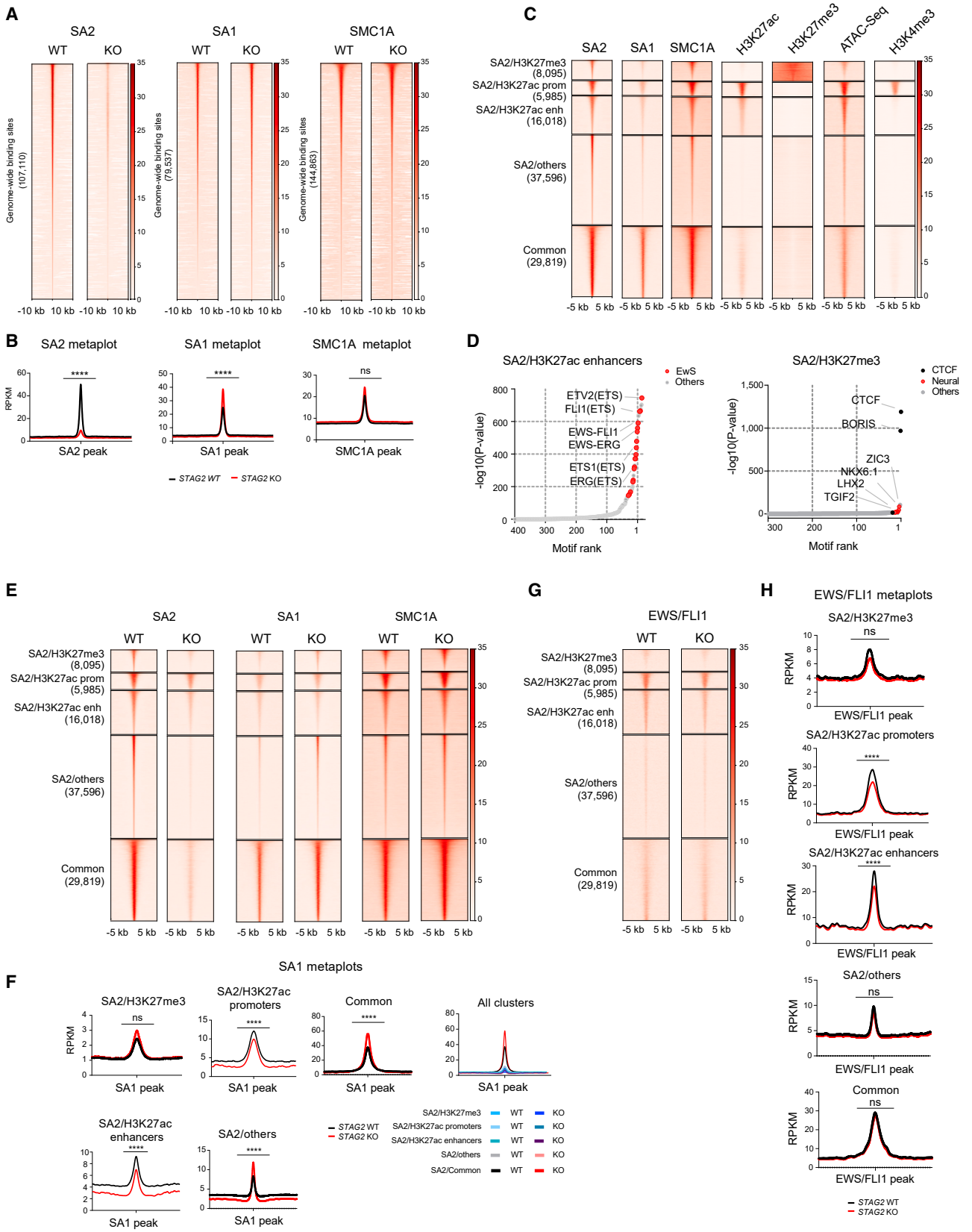

(legend on next page)

and 2B). There was a trend toward increased levels of SMC1, although this did not reach statistical significance.

Previous studies have shown that the two cohesin complexes bind to common as well as non-overlapping regions (Cuadrado et al., 2019; Kojic et al., 2018; Ochi et al., 2020). While cohesin-SA1 often colocalizes with CTCF and cohesin-SA2 at TAD boundaries, cohesin-SA2 occupies regulatory regions replete with cell-type-specific enhancers. Therefore, we set out to determine where cohesin-SA2 resides with respect to putative regulatory genomic domains defined by chromatin accessibility and the histone modification marks H3K27ac, H3K27me3, and H3K4me3 associated with enhancers, polycomb repressive complex, and active promoters, respectively. Our results showed that STAG2-bound regions cluster into five discrete categories. Four of the regions contained high levels of cohesin-SA2 along with either H3K27me3 (SA2/H3K27me), H3K27ac (SA2/H3K27ac-Promoters, SA2/H3K27ac_Enhancers), or without either mark (SA2/Others), whereas the last group has high levels of cohesin-SA1 and cohesin-SA2 (common) (Figure 2C). Motif enrichment analysis revealed that regions bound by cohesin-SA2 and decorated by the H3K27ac mark, both at promoters and enhancers, are enriched with canonical ETS motifs (Figures 2D and S2A). In light of the role played by EWS/FLI1 in Ewing sarcoma, these data suggest that cohesin-SA2 may partner with the fusion oncogene to hijack and reprogram the gene-regulatory landscape. Importantly, while the cohesin-SA2/Others, common, and SA2/H3K27me3 regions were all enriched for the canonical motifs of CTCF and its paralog BORIS (CTCF-like), several neurogenic transcription factors were also enriched in the SA2/H3K27me3 region, suggesting that cohesin-SA2 may contribute to the regulation of neurodevelopmental programs in Ewing sarcoma (Figures 2D and S2A).

Next, we determined how binding of the cohesin subunits changes across these predefined regions as a consequence of STAG2 depletion. As expected, the binding signal for STAG2 decreased significantly across all regions (Figure S2B). Strikingly, STAG1 and SMC1A binding increased significantly, or with a trend toward significance, in all regions with the exception of SA2/H3K27ac region, suggesting that cohesin-SA1 does not sufficiently replace cohesin-SA2 around a subset of enhancers and promoters (Figures 2E, 2F, and S2C). Given the significant enrichment of several ETS motifs in the cohesin-SA2/H3K27ac regions, we also tested whether deletion of *STAG2* affects the distribution of EWS/FLI1 on chromatin. Consistent with the results of the motif enrichment analysis, EWS/FLI1 binding was the strongest at cohesin-SA2-bound enhancer/promoter-marked regions and was mostly absent at H3K27me3-marked regions (Figure 2G). Deletion of *STAG2* modestly decreased the binding of EWS/FLI1 genome-wide and more prominently at H3K27ac-marked regions, without affecting the expression levels of the fusion oncoprotein itself (Figures 2G, 2H, and S2D–S2F).

Deletion of STAG2 disrupts long-range *cis* enhancer-promoter interactions, including those anchored by EWS/FLI1

To evaluate how loss of STAG2 affects cohesin-mediated *cis*-chromatin interactions across the genome, we next performed proximity ligation-based global chromatin conformation profiling by SMC1A HiChIP in control and *STAG2* KO A673 cells. Our analysis identified a total of 56,219 high-confidence, cohesin-anchored, chromatin interactions out of which 4,500 display significantly altered contact frequency in *STAG2* KO cells relative to WT controls (Figure 3A and Table S1). Importantly, more than one-third of these altered loops are anchored by a putative enhancer on one end and a gene promoter on the other (Figure 3B and Table S1). The data also revealed that chromatin regions that are furthest from each other are more likely to decrease in contact frequency, whereas loops established by closely located interacting pairs are enriched for increase in contact frequency as a result of STAG2 loss (Figure 3C). Notably, roughly 23% of the differential loops involve anchor points that hosted long-range contacts that both increase and decrease in frequency of interaction, suggesting a role for loop reorganization in a subset of cases.

Given the significant number of altered loops connecting enhancers to promoters, we next asked which sequence-specific transcription factors are likely to preferentially engage these enhancers and mediate long-range chromatin contacts. Motif enrichment analysis identified consensus binding sequences for the dominant oncogenic fusion transcription factor EWS/FLI1, as well as the ETS family members ETS1 and ERG, among the top ten enriched motifs (Figure 3D and Table S2). Thus, we hypothesized that deletion of *STAG2* may also disrupt EWS/FLI1 anchored long-range chromatin contacts.

To test this hypothesis, we performed ChIP-seq and mapped the genome-wide binding pattern of EWS/FLI1, and overlapped our peaks with two additional studies performed by other

Figure 2. STAG2 occupies PRC2- and enhancer-marked regions, and its deletion is incompletely compensated by STAG1

(A) Genome-wide heatmaps of SA2, SA1, and SMC1A ChIP-seq peak centered signal in A673 cells expressing WT or KO *STAG2*. Regions are ranked based on WT signal.

(B) Read density metaplots showing average RPKM (reads per kilobase per million)-normalized signal for SA2, SA1, and SMC1A in WT (black) and *STAG2* KO (red) A673 cells. Differential read density in KO versus WT conditions. Unpaired t test with Welch's correction, ****$p < 0.0001$; ns, not significant.

(C) Clustered heatmaps of ChIP-seq peak centered signal for SA2, SA1, SMC1A, H3K27ac, H3K27me3, chromatin accessibility (ATAC-seq), and H3K4me3. Cluster regions are ranked by SA2 signal.

(D) Hockey plots depicting motifs enriched in SA2/H3K27ac enhancers and SA2/H3K27me3 regions defined in (C).

(E) Clustered heatmaps depicting SA2, SA1, and SMC1A signal in the cohesin regions defined in (C) in control and *STAG2* KO A673 cells.

(F) Metaplots showing average SA1 signal in the cohesin regions defined in (C). Differential read density in KO versus WT conditions. Unpaired t test with Welch's correction, ****$p < 0.0001$, **$p < 0.01$.

(G) Clustered heatmap depicting EWS/FLI1 signal in cohesin regions defined in (C) in control and *STAG2* KO A673 cells.

(H) Metaplot showing average EWS/FLI1 signal in cohesin regions defined in (C). Differential read density in KO versus WT. Unpaired t test with Welch's correction, ****$p < 0.0001$, **$p < 0.01$.

See also Figure S2.

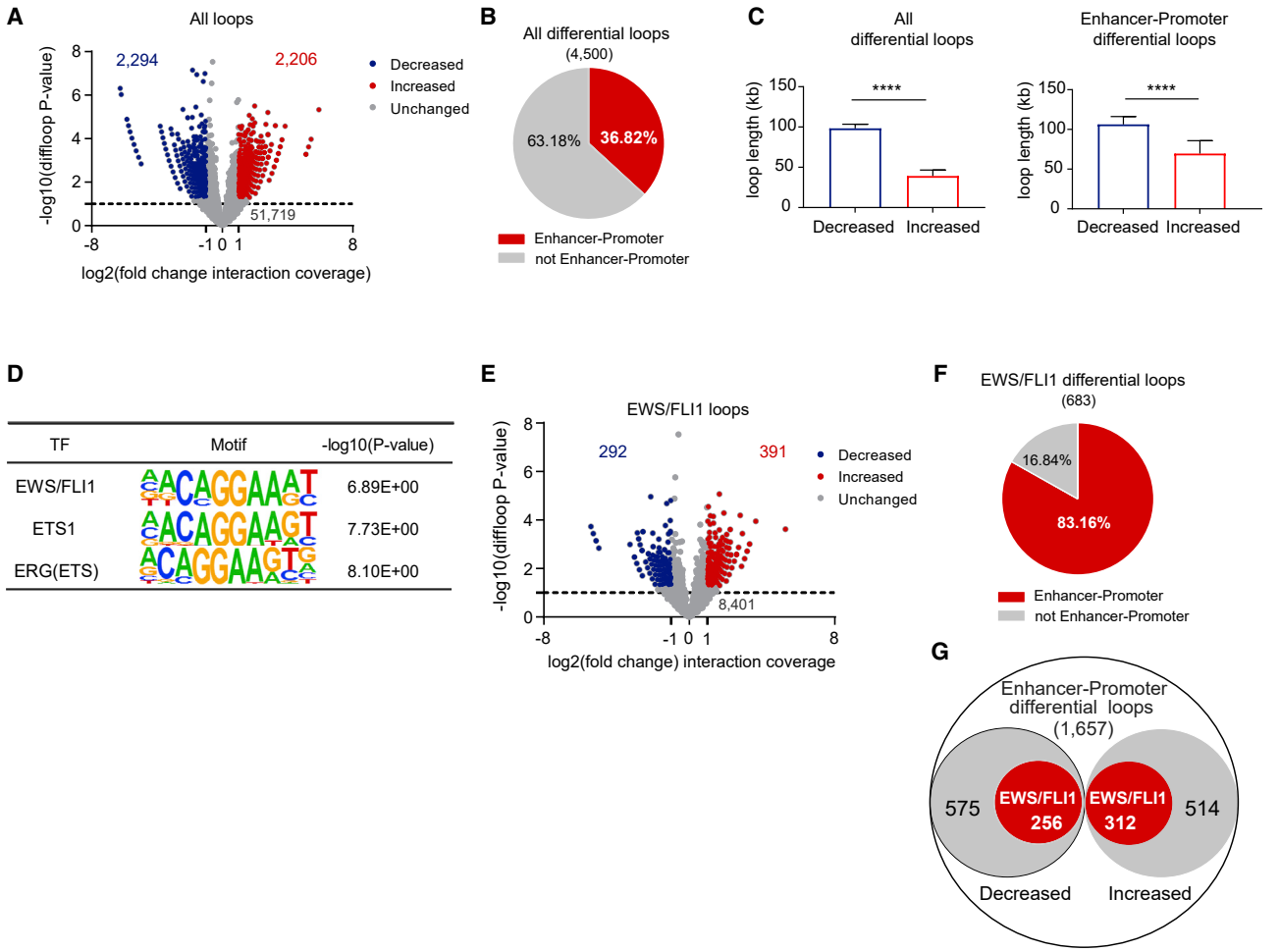

Figure 3. Loss of *STAG2* alters the frequency of *cis*-chromatin contacts

(A) Volcano plot of changes in chromatin loop strength comparing *STAG2* WT with KO A673 cells based on SMC1A HiChIP. EdgeR overdispersed Poisson regression, $|(FC)| \geq 2$, $p \leq 0.05$.

(B) Pie chart depicting the fraction of differential loops involving enhancer-promoter interactions. Two-tailed Fisher's exact test, ****$p < 0.0001$.

(C) Median + 95% confidence interval plots for lengths of differential loops. Unpaired t test with Welch's correction, ****$p < 0.0001$.

(D) Three of the top ten enriched motifs for the enhancer regions involved in differential enhancer-promoter loops.

(E) Volcano plot depicting the differential status of the 9,084 EWS/FLI1 anchored differential loops. EdgeR overdispersed Poisson regression, $|FC| \geq 2$, $p \leq 0.05$.

(F) Pie chart depicting the fraction of EWS/FLI1 anchored differential loops involving enhancer-promoter interactions. Two-tailed Fisher's exact test, ****$p < 0.0001$.

(G) Diagram depicting the fraction of EWS/FLI1 anchored enhancer-promoter interactions as a subset of all differential enhancer-promoter loops. Two-tailed Fisher's exact test, ****$p < 0.0001$.

See also Figure S3; Tables S1 and S2.

investigators in A673 cells (Riggi et al., 2014; Tomazou et al., 2015). We integrated these high-confidence binding sites with H3K27ac ChIP-seq, chromatin accessibility, and GGAA repeat calling from the reference genome to generate a comprehensive view of EWS/FLI1 binding. As expected, EWS/FLI1 bound strongly at promoters, canonical enhancers, and enhancers associated with long GGAA microsatellite repeats (Figure S3A). We then asked whether the cohesin complex also binds to these regions to potentially mediate long-range interactions and whether cohesin loading, as well as EWS/FLI1 binding, change in the context of STAG2 loss. Our data revealed that SMC1A and the H3K27ac mark strongly colocalize with EWS/FLI1 at enhancers and promoters (Figure S3B). Importantly, consistent with our previous observations (Figures 2F and 2H), in *STAG2* KO cells EWS/FLI1 binding decreased across multiple regions, with the exception of GGAA repeat-marked enhancers, while STAG1 failed to compensate for the loss of STAG2 across all of the EWS/FLI1-bound regions assessed (Figure S3C). Notably, cohesin loading at EWS/FLI1-bound enhancers, particularly at GGAA repeats, is highly selective for Ewing sarcoma cells, as we found very low signal for SMC1A or SMC3 binding at these sites in multiple other cell types (Figure S3D). Combined, these results argue that cohesin and EWS/FLI1 cooperatively establish and drive part of the oncogenic enhancer-promoter network in

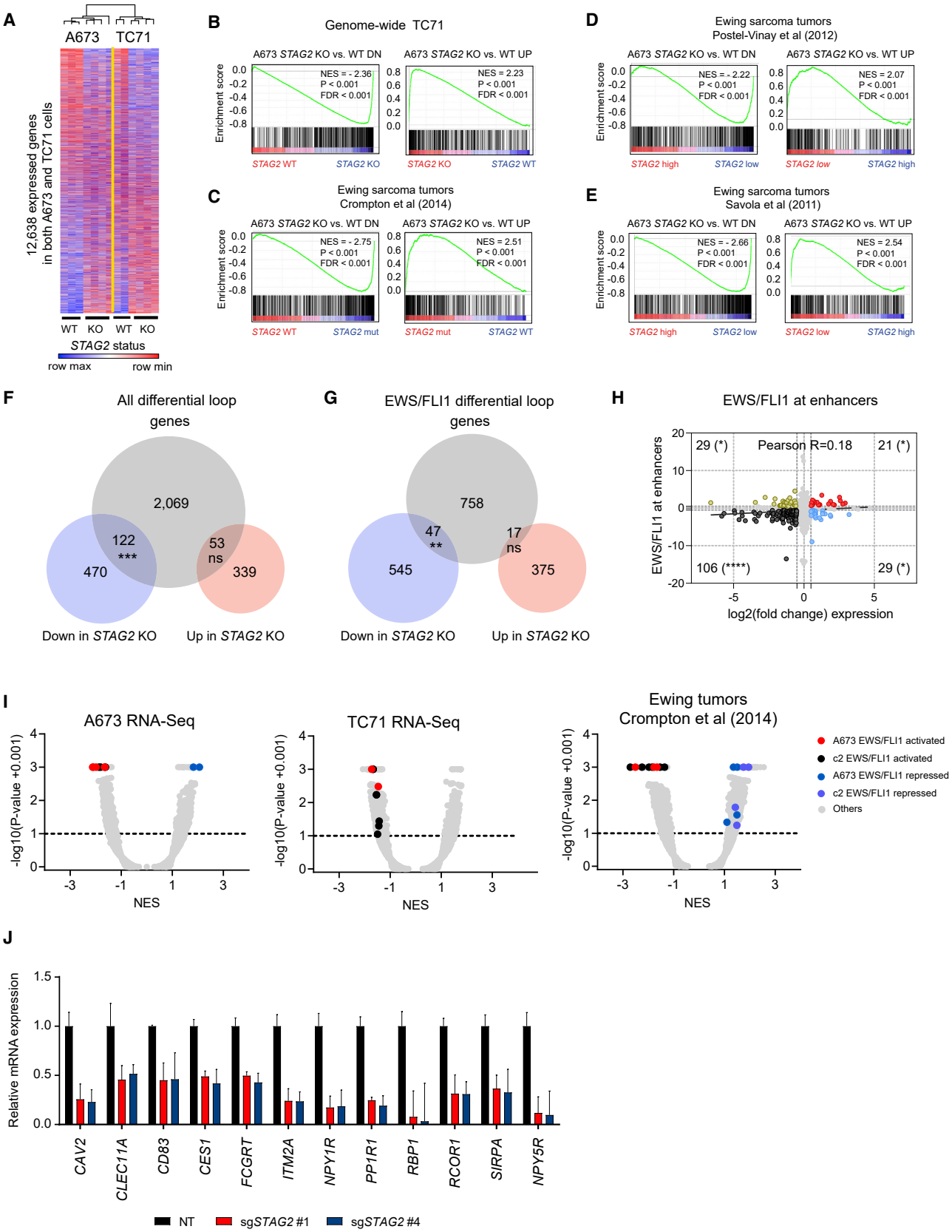

(legend on next page)

Ewing sarcoma and that the loss of STAG2 may decommission the components necessary for maintaining these interactions.

Next, we interrogated our HiChIP data to identify long-range chromatin contacts that are anchored at least at one edge by EWS/FLI1 and cohesin. Our analysis identified a total of 9,084 high-confidence loops that satisfy this criterion (Figure 3E and Table S1). In STAG2-depleted cells, there were 683 EWS/FLI1 anchored loops that significantly changed in contact frequency. Strikingly, 83.16% of these loops connected enhancers to promoters with EWS/FLI1 occupying the edge of the loop located at the distal enhancer site (Figure 3F and Table S1). Moreover, as a group, EWS/FLI1 anchored loops accounted for a large subset of all significantly altered enhancer-promoter contacts in *STAG2* KO cells (Figure 3G). Similar to all other altered loops, long-range chromatin contacts mediated by EWS/FLI1 also tend to decrease in contact frequency the further apart interacting regions are (Figure S3C). Thus, in aggregate, these findings strongly suggest that loss of STAG2 significantly modifies *cis*-chromatin interactions and may partially reprogram the oncogenic program driven by EWS/FLI1.

Deletion of *STAG2* rewires the transcriptional program of Ewing sarcoma cells

Given the significant changes we observed in the frequency of enhancer-promoter interactions and the important functional role they play in regulating gene expression, we predicted that loss of STAG2 will have a measurable effect on transcriptional output. To test this idea, we performed RNA sequencing (RNA-seq) analysis in two independent Ewing sarcoma cell lines where we deleted *STAG2*. We found that loss of STAG2 causes a similar pattern of transcriptional changes in both cell lines (Figure 4A and Table S3) with a high degree of overlap between the genes, whose expression changed significantly ($|\log_2$(fold change [FC])$| \geq 1.5$, adjusted $p \leq 0.1$, Figure S4A). Moreover, gene set enrichment analysis (GSEA) revealed highly concordant transcriptional changes in TC71 and A673 cells (Figures 4B and S4B). Finally, to determine whether the transcriptional changes seen in our cell-line models are generalizable and reflective of a conserved biology that emerges as a consequence of STAG2 loss, we performed GSEA using three independent gene expression datasets of primary Ewing sarcoma patient tumors (Crompton et al., 2014; Postel-Vinay et al., 2012; Savola et al., 2011). Our analysis revealed that the differentially expressed genes in each of the two cell lines were significantly enriched in the transcriptomes of patient tumors that carry mutant *STAG2* or express low levels (Figures 4C–4E and S4C–S4E). Collectively, these findings indicate that loss of STAG2 produces highly consistent and stable transcriptional changes that may undergo selection to confer a competitive advantage.

The observation that enhancer-promoter interactions and transcriptional programs are concurrently altered in *STAG2* KO cells prompted us to investigate whether the two are directly linked. To this end, we selected all the differential loops that are anchored within 5 kb of a transcriptional start site (TSS) and annotated the nearest expressed gene. We identified 2,000 loops and the associated genes (differential loop genes) that satisfied the criteria. Using this list, we interrogated our transcriptional data generated in A673 cells focusing only on genes that undergo significant change in expression ($|\log_2(FC)| \geq 1.5$, adjusted $p \leq 0.1$) in the context of STAG2 loss. This integrative analysis of HiChIP and RNA-seq data identified a significant association between loss of gene expression and altered cohesin-mediated *cis*-chromatin interactions (Figure 4F and Table S3). Indeed, nearly 20% of genes repressed in STAG2-depleted cells also display differential chromatin loops proximal to their transcriptional start sites. Notably, genes upregulated upon *STAG2* deletion did not have a statistically significant association with the presence of an altered loop near their promoters. Given the substantial number of altered chromatin contacts we identified that are anchored by EWS/FLI1, we expanded our analysis for the subset of genes that are associated with these loops. We identified a total of 822 genes that are associated with differential EWS/FLI1 anchored loops. Importantly, the results similarly showed that there is a significant association with the presence of an altered loop near the TSS of downregulated but not upregulated genes in *STAG2* KO cells (Figures 4G and S4F; Table S3). Taken together, these results show that the cohesin complex anchors critical chromatin loops near gene promoters and that the loss of STAG2 disrupts these structures to produce consistent and stable changes to genetic programs that may drive tumorigenesis.

STAG2 loss attenuates the EWS/FLI-dependent oncogenic program

EWS/FLI1 is a dominant oncogenic fusion transcription factor and, as such, drives a defined genetic program in Ewing sarcoma cells. Given the alterations we observed in its binding at enhancer-marked regions, chromatin contacts involving

Figure 4. Loss of *STAG2* alters the EWS/FLI1-driven oncogenic transcriptional program

(A) Heatmap and average linkage dendrogram of genome-wide gene expression, $\log_2$(normalized counts), in *STAG2* KO versus WT A673 and TC71 cells.

(B–E) GSEA plots demonstrating the enrichment of the *STAG2* KO versus WT gene signature for A673 cells in the genome-wide expression changes induced by *STAG2* KO in (B) TC71 cells or (C–E) three distinct Ewing sarcoma primary patient tumor datasets. Normalized enrichment score, p value, and false discovery rate (FDR) are indicated in each plot.

(F) Venn diagram depicting the overlap between differentially expressed genes with genes harboring a differential loop within 5 kb of their TSS. Two-tailed Fisher's exact test, ***$p < 0.001$; ns, not significant.

(G) Similar analysis as in (F) is shown for EWS/FLI1 anchored differential loops. Two-tailed Fisher's exact test, **$p < 0.01$; ns, not significant.

(H) Scatterplot depicting the overlap between gene expression change and EWS/FLI1 binding at the nearest enhancer assessed by ChIP-seq. Two-tailed Fisher's exact test, ****$p < 0.0001$, *$p < 0.05$.

(I) Volcano plots for GSEA enrichment scores for the genome-wide expression changes induced in A673 and TC71 and by *STAG2* mutant versus *STAG2* WT tumor samples from Crompton et al. (2014) versus the union of a collection of 12 EWS/FLI1 public gene signatures in A673 cells and MSigDB v7.1 c2 pathways (5,529 gene sets).

(J) qRT-PCR-based validation of a subset of EWS/FLI1 target genes repressed in *STAG2* KO relative to control A673 cells. Data shown as mean ± SD.

See also Figure S4 and Table S3.

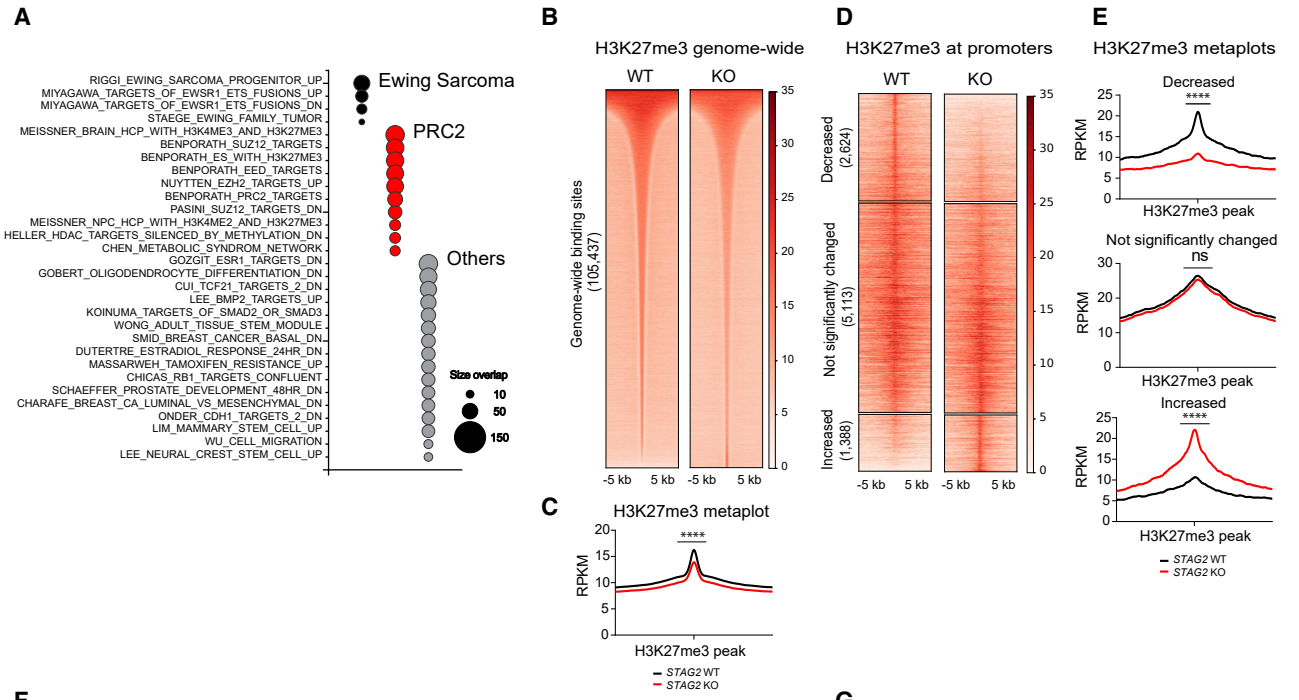

H

#	TF	Motif	-log10(P-value)
1	Pdx1 (Homeobox)		9.91E+00
2	PBX2 (Homeobox)		6.84E+00
3	Pit1+1bp (Homeobox)		6.17E+00
4	HOXB13 (Homeobox)		5.16E+00
5	Oct2 (POU,Homeobox)		4.89E+00
6	HOXA1 (Homeobox)		4.89E+00
7	HOXA2 (Homeobox)		4.85E+00
8	PBX3 (Homeobox)		4.38E+00
9	CUX1 (Homeobox)		4.16E+00
10	Oct6(POU,Homeobox)		3.97E+00

Figure 5. Loss of *STAG2* perturbs PRC2-mediated regulation of gene expression

(A) Bubble plot summarizing top significant enrichments (size overlap ≥25, p ≤ 0.05, FDR ≤ 0.05) for the MSigDB v7.1 c2 collection. Enriched gene sets are clustered in representative functional categories.

(B) Genome-wide heatmaps of H3K27me3 ChIP-seq signal in A673 cells expressing WT or *STAG2* KO centered on significant peaks identified in either or both conditions.

(legend continued on next page)

enhancers and promoters anchored by EWS/FLI1, and their significant association with at least downregulated genes, we sought to determine the extent to which STAG2 loss specifically perturbs the EWS/FLI1-dependent oncogenic program. To directly test this idea, we initially evaluated the relationship between the change in EWS/FLI1 binding as assessed by ChIP-seq and the level of change in expression of the nearest gene. Our analysis revealed that on average more genes lose EWS/FLI1 binding and are repressed in *STAG2* KO cells relative to controls (Figure S4G). Importantly, EWS/FLI1 binding loss at enhancers, but not at promoters, significantly correlated with downregulation of gene expression (Figures 4H and S4H).

Next, we generated a robust list of EWS/FLI1-dependent gene expression signatures by utilizing several previously published studies (Table S4). Using this refined compendium of EWS/FLI1 signatures, we performed GSEA on the transcriptome of *STAG2* KO cells. Intriguingly, in both A673 and TC71 cells, loss of STAG2 markedly repressed the EWS/FLI1-dependent oncogenic program (Figures 4I and S4I). Similar analysis performed in three independent Ewing tumor datasets also showed attenuation of the oncogenic program as a consequence of *STAG2* mutation (Figures 4I and S4I; Table S4). Furthermore, we took advantage of a recently generated single-cell RNA-seq-based transcriptomic signature of EWS-FLI1 dubbed IC-EwS (Aynaud et al., 2020), and performed GSEA on our *STAG2* KO cell lines and *STAG2* mutant primary tumors. Consistent with the results generated using our refined compendium of signatures, the IC-EwS signature was significantly repressed in *STAG2* KO and *STAG2* mutant cells, further confirming that loss of STAG2 dominantly limits part of the oncogenic program (Figure S4J). Finally, we performed qRT-PCR and validated the suppression of a number of EWS/FLI1 target genes in *STAG2* KO cells relative to controls (Figure 4J). Combined, the results of these studies strongly argue that STAG2 loss modulates the EWS/FLI1 oncogenic program, in part through disruption of long-range chromatin contacts anchored by EWS/FLI1.

Polycomb repressive complex-mediated gene regulation is disrupted in *STAG2* KO cells

To gain a broader insight into the transcriptional changes induced by loss of STAG2, we next performed a comprehensive enrichment analysis using gene sets available through the Molecular Signatures Database (MSigDB) collection. Our results further confirmed that Ewing sarcoma- and EWS/FLI1-specific programs are altered in *STAG2* KO cells, as we found four Ewing sarcoma-related signatures out of the top 50 gene sets (Figure 5A and Table S5). Strikingly, we also found several PRC2-associated gene signatures as significantly enriched in our transcriptional data, suggesting that deletion of *STAG2* likely disrupts PRC2-mediated regulation of gene expression (Figure 5A and Table S5). To directly assess the involvement of PRC2-dependent epigenetic dysregulation, we first performed calibrated ChIP-seq for the PRC2 modification mark H3K27me3 in control and *STAG2* KO cells. We found that the level of H3K27me3 mark is decreased in *STAG2* KO cells genome-wide (Figures 5B and 5C). Importantly, the PRC2 mark is enriched at a subset of genomic regions preferentially occupied by cohesin-SA2, and these regions also lose H3K27me3 significantly in *STAG2* KO cells (Figures S5A and S5B).

The PRC2 complex often localizes near gene promoters to regulate transcription. Thus, we evaluated how the H3K27me3 mark changes, specifically within 3 kb of the TSS in the context of STAG2 loss. We identified 2,624 sites with decreased and 1,388 sites with increased levels of H3K27me3 (Figures 5D and 5E). To determine whether these changes are associated with, and thus likely to regulate, gene expression, we assessed the degree of overlap between differentially expressed genes ($|\log_2(FC)| \geq 1.5$, adjusted $p \leq 0.1$) and genes with altered levels of H3K27me3 at the promoter. Our analysis revealed a strong correlation between gene expression and levels of H3K27me3 at the promoter (Figure 5F). Indeed, we identified 107 genes that were repressed with significant promoter proximal deposition of H3K27me3 and 60 genes that were induced in *STAG2* KO cells that concurrently lost the PRC2 mark (Figure 5F). Next, we asked whether changes to *cis*-chromatin contacts in the proximity of gene promoters are associated with altered levels of H3K27me3 in the subset of genes that were differentially expressed. Our analysis revealed a lack of any statistically significant correlation, suggesting that the change in PRC2-mediated regulation of gene expression in the wake of STAG2 loss is likely independent of alterations to long-range enhancer-promoter interactions (Figure 5G). Notably, although we did not find changes in the levels of H3K27ac genome-wide in *STAG2* KO cells, we found a very strong inverse correlation between the levels of H3K27me3 and H3K27ac levels at the promoters of differentially expressed genes (Figures S5C–S5G), suggesting that active epigenetic modification is taking place in the vicinity of the TSS. We thus decided to check whether this is mediated by a few select transcription factors. To test the idea, we performed motif enrichment analysis using the genomic sequences that were differentially marked by H3K27me3 near the promoter for all genes. Interestingly, our analysis revealed the enrichment of a number of Homeobox and POU family pioneer neurodevelopmental transcription factors (Figure 5H and Table S6). These results suggest that loss of STAG2 may perturb PRC2-mediated regulation of developmental programs.

(C) Metaplots showing average genome-wide H3K27me3 signal in *STAG2* KO and WT A673 cells. Unpaired t test with Welch's correction, ****$p < 0.0001$.
(D) Clustered heatmaps depicting TSS ± 5-kb promoter regions with decreased, not significantly changed, or increased H3K27me3 ChIP-seq binding in *STAG2* KO versus WT A673 cells (|Delta(area under curve signal)| ≥ 1.5).
(E) Metaplots showing average H3K27me3 signal in the promoter regions defined in (C). Differential read density for *STAG2* KO versus WT A673 within clusters. Unpaired t test with Welch's correction, ****$p < 0.0001$; ns, not significant.
(F) Scatterplot depicting the overlap between the genes with significant change for H3K27me3 ChIP-seq binding at promoter regions with differentially expressed genes. Two-tailed Fisher's exact test, ****$p < 0.0001$; ns, not significant.
(G) Venn diagram showing the overlap between the subset of genes with concurrent changes in expression and H3K27me3 levels at the promoter (shown in F) with the total list of genes harboring a differential loop within 5 kb of the TSS. Two-tailed Fisher's exact test; ns, not significant.
(H) List of top ten enriched motifs at the promoters of genes with altered H3K27me3 levels in *STAG2* KO cells.
See also Figure S5; Tables S5 and S6.

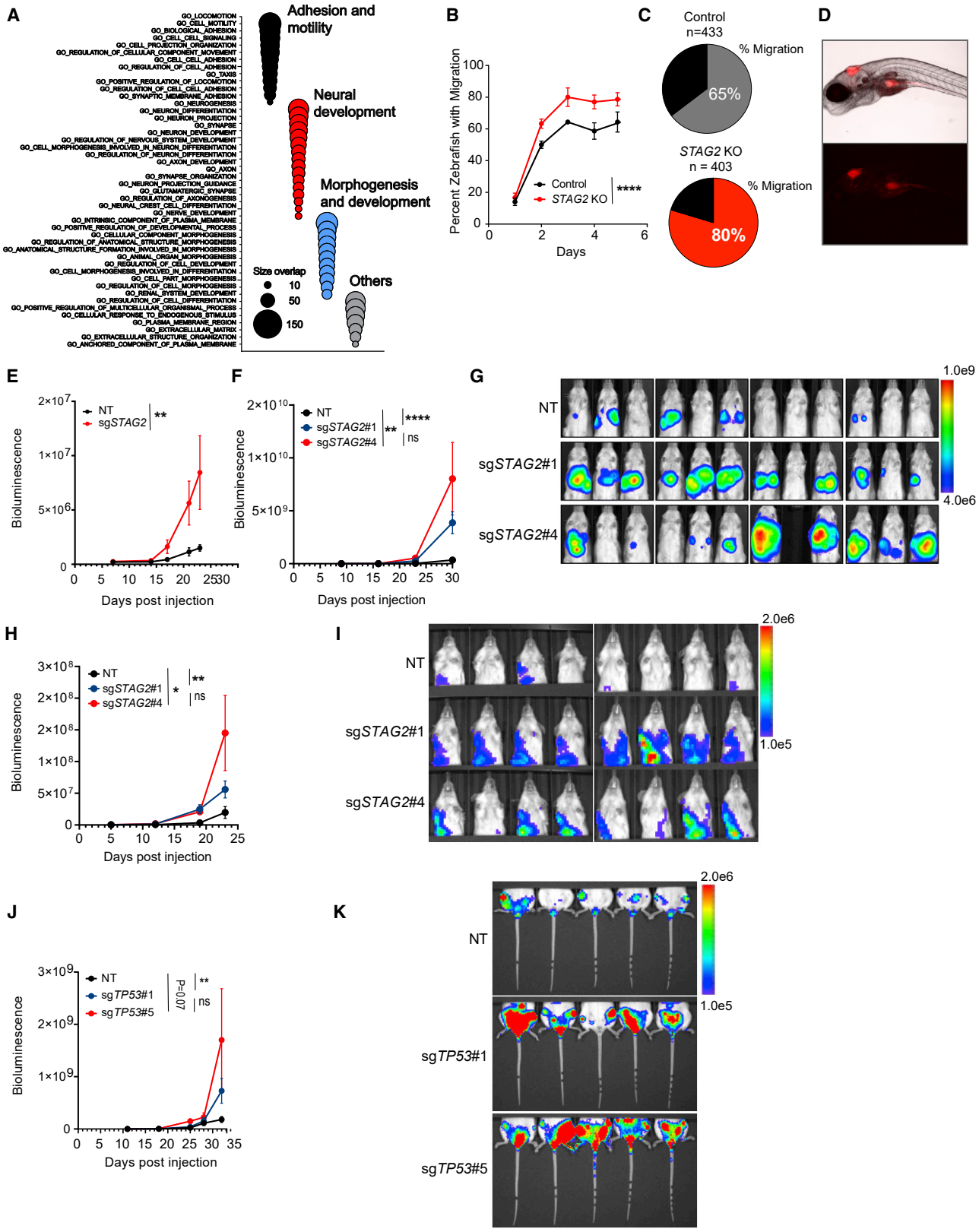

(legend on next page)

STAG2 loss reprograms migratory and neurodevelopmental transcriptional programs

Our data thus far highlight changes in the enhancer-promoter interaction network, a partial dampening of the EWS/FLI1-dependent oncogenic transcriptional program, and disruption of PRC2-mediated regulation of gene expression as key emergent molecular manifestations of STAG2 loss. To gain insight into the potential functional outcomes of these changes, we performed gene ontology (GO) analysis, which leverages transcriptional signatures to infer cellular processes that uniquely define the network of differentially expressed genes. Our data revealed the striking enrichment of three functional categories in the top 50 GO signatures (Figure 6A and Table S7). First, we identified several processes indicative of an altered invasive and migratory behavior as exemplified by GO terms such as locomotion, motility, taxis, and biological adhesion. Second, we observed a strong enrichment of early developmental and morphogenetic processes. Third and likely a subcategory of the second feature, we identified a robust enrichment of neurodevelopmental processes including the GO terms neurogenesis, neuron differentiation, neuron projection, and axon development. Thus, at the cellular level depletion of STAG2 appears to alter the migratory potential of Ewing sarcoma, along with the hijacking and reprogramming of early developmental programs that may reinforce these properties.

Given the enrichment of cell motility-associated signatures, we next sought to evaluate the migratory potential of Ewing sarcoma cells. The zebrafish provides a robust model system to accurately track fluorescently labeled cells *in vivo* (El-Naggar et al., 2015; Olson and Nechiporuk, 2018). Thus, we injected control and *STAG2* KO cells into the hindbrain of zebrafish larvae (control n = 433, *STAG2* KO n = 403) 2 days post fertilization and monitored the movement of cells daily for 5 additional days via microscopy (Figure S6A). For controls, we injected fluorescently labeled microspheres and confirmed that there is no passive diffusion up to 5 days post injection (Figure S6B). At each time point, we scored colonization of the dorsal surface, yolk sac, and tail. We observed enhanced migration of *STAG2* KO cells, which migrated to at least one distal site in 85% of the zebrafish injected, whereas *STAG2* WT cells only did so in 65% of the cases (Figures 6B–6D).

STAG2 loss enhances the metastatic potential of Ewing sarcoma xenografts

Based on the transcriptional signature we identified, the results of the migration assay in zebrafish, and the reported clinical association between loss-of-function mutations in *STAG2* and the incidence of metastasis (Crompton et al., 2014), we hypothesized that deletion of *STAG2* will enhance the metastatic potential of Ewing sarcoma cells. To test this hypothesis, we performed extensive xenograft studies by transplanting control and *STAG2* KO Ewing sarcoma cells into immunocompromised NSG mice. First, we generated polyclonal *STAG2* KO TC71 cells and injected them via tail vein into recipient mice (Figure S6C). While the overall disease burden was similar, *STAG2* KO cells metastasized significantly more to the hindleg bone marrow space relative to controls (Figures 6E and S6D–S6H). Next, we used clonally selected control and *STAG2* KO A673 cells and transplanted them via tail vein into recipient mice. In this model we measured the extent of metastasis to visceral organs. We observed significantly more infiltration of lungs and liver tissue in *STAG2* KO recipient mice compared with controls (Figures 6F and 6G). Finally, we employed a semi-orthotopic xenograft model by transplanting cells into the hindleg intramuscular space. The data revealed that *STAG2* KO A673 cells grow more aggressively at the primary site (Figures S6I and S6J) and also metastasized to distal organs better than their WT counterparts (Figures 6H and 6I). We further confirmed the finding by *ex vivo* imaging of lungs recovered from recipient mice at the study endpoint (Figures S6K and S6L).

STAG2 and *TP53* mutations are often concurrent and carry a dismal clinical outcome (Tirode et al., 2014). Both A673 and TC71 cells, which we have used for most of our studies, are mutants for *TP53*. Thus, we asked whether deletion of *TP53* in the background of *STAG2* mutation can further modulate disease course *in vivo*. To this end, we utilized TC32 cells, which are mutant for *STAG2* but carry a WT copy of *TP53*. We transplanted control and *TP53*-deleted cells via tail vein injection into recipient mice and measured the disease course by bioluminescence imaging. We observed that *TP53* KO cells generate a significantly more aggressive disease (Figures S6M and S6N) associated with higher infiltration of hindlegs and lungs (Figures 6J, 6K, S6O, and S6P). Taken together, the results of our studies

Figure 6. Depletion of *STAG2* enhances the migration and metastatic potential of Ewing sarcoma cells

(A) Bubble plot summarizing top 50 significant enrichments (size overlap $\geq$10, p $\leq$ 0.05, FDR $\leq$ 0.05) for the MSigDB v7.1 c5 collection. Enriched gene sets are clustered in representative functional categories.

(B) Line graph represents mean ± SD of the percentage of zebrafish that displayed migration to at least one of the three regions of interest as a function of the days post injection. Two-way ANOVA, ****p < 0.0001.

(C) Pie chart showing the percentage of zebrafish with migration of Ewing cells to at least one of the three sites examined 3 days post injection.

(D) Representative bright-field (top) and fluorescence (541/565 nm bottom) images displaying migration of TC71 cells to the yolk sac.

(E) Quantification of bioluminescence signal collected for lower extremities after blocking upper abdominal cavity. Line graph represents mean ± SEM, n = 8 per group. Two-way ANOVA, **p < 0.001.

(F) Quantification of bioluminescence signal collected for upper thoracic cavity after blocking lower abdomen. Line graph represents mean ± SEM, n = 12 per group. Two-way ANOVA, ****p < 0.0001,**p < 0.01; ns, not significant.

(G) Bioluminescence images of mice described in (F).

(H) Quantification of bioluminescence signal collected for upper thoracic cavity while blocking lower abdomen. Line graph represents mean ± SEM, n = 8 per group. Two-way ANOVA, ****p 0.0001,**p < 0.01; ns, not significant.

(I) Bioluminescence images of mice described in (H).

(J) Quantification of bioluminescence signal collected for lower extremities after blocking upper abdominal cavity. Line graph represents mean ± SEM, n = 5 per group. Two-way ANOVA, **p < 0.01; ns, not significant.

(K) Bioluminescence images of mice described in (J).

See also Figure S6 and Table S7.

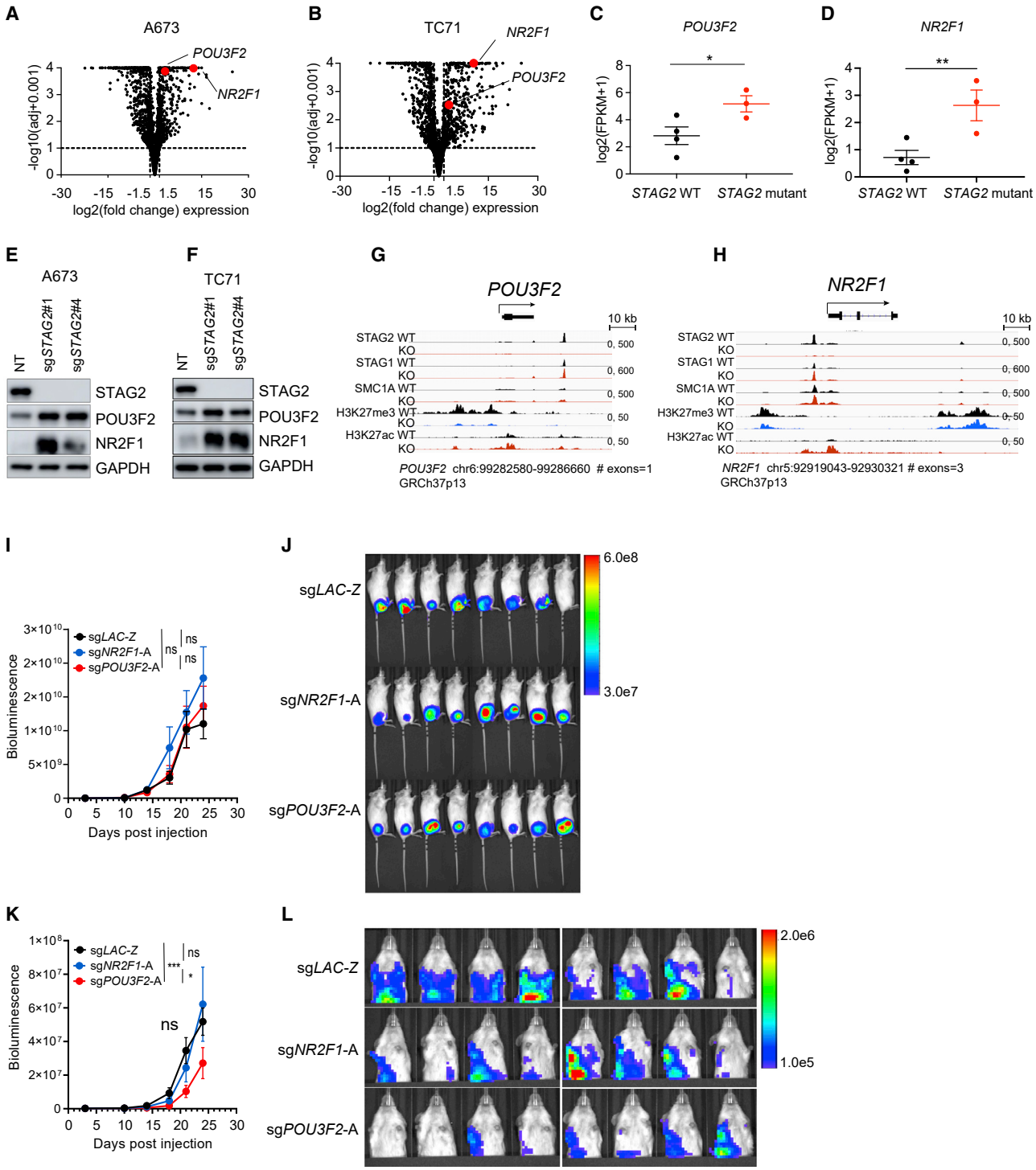

Figure 7. The neurodevelopmental transcription factor POU3F2 modulates the metastatic potential of STAG2 KO Ewing sarcoma cells

(A and B) Volcano plot depicting the transcriptional changes induced by *STAG2* KO versus control in (A) A673 and (B) TC71 cells. *POU3F2* and *NR2F1* are highlighted in red. Significance cutoffs: $|\log_2(FC)| \geq 1.5$, adjusted $p \leq 0.10$.

(C and D) Scatter dot plot depicting the mean ± SEM mRNA $\log_2$(FPKM [fragments per kilobase per million] + 1) expression of (C) *POU3F2* and (D) *NR2F1* in three *STAG2* mutant tumors versus the top four *STAG2* WT tumors with highest *STAG2* expression from Crompton et al. (2014) data. Mann-Whitney non-parametric t test, $^{**}p < 0.001$, $^{*}p < 0.05$.

(E and F) Validation of an increase in POU3F2 and NR2F1 protein levels in (E) A673 and (F) TC71 cells clonally selected for *STAG2* loss.

(G and H) Integrated genomics viewer track showing SA2, SA1, SMC1, H3K27me3, and H3K27ac signals at the (G) *POU3F2* and (H) *NR2F1* locus in control and *STAG2* KO A673 cells.

(legend continued on next page)

strongly argue for a role for *STAG2* loss in promoting metastatic behavior *in vivo* and also provide experimental evidence for the clinical associations observed previously.

The neurodevelopmental transcription factor POU3F2 modulates the metastatic potential of *STAG2*-deleted Ewing sarcoma cells

To identify critical mediators of metastatic behavior downstream of STAG2, we focused on genes that were induced in the wake of STAG2 depletion. Two neurodevelopmental transcription factors, *POU3F2* and *NR2F1*, were consistently upregulated in *STAG2* KO cells relative to controls (Figures 7A and 7B). POU3F2 is a pioneer transcription factor critical for early neuroepithelial progenitor specification and linked to metastatic properties in multiple tumor types (Bishop et al., 2017; Fane et al., 2019; Urban et al., 2015; Yao et al., 2017; Zeng et al., 2018). Likewise, NR2F1 is an orphan nuclear receptor important for many aspects of neurogenesis and implicated in tumor cell dormancy, invasion, and metastasis (Armentano et al., 2006, 2007; Gao et al., 2019; Sosa et al., 2015; Zhou et al., 1999). Therefore, we decided to investigate the potential role of these two transcription factors in modulating the metastatic capacity of Ewing sarcoma cells.

Consistent with our findings in cell-line models, *STAG2* mutant Ewing tumors express elevated levels of *POU3F2* and *NR2F1* relative to controls (Figures 7C, 7D, and S7A–S7D). We further confirmed these results by western blot analysis in both clonally selected and polyclonal *STAG2* KO A673 and TC71 cells (Figures 7E, 7F, S7E, and S7F). The expression of lineage-specifying transcription factors is often regulated by the polycomb repressive complex. In agreement with this notion, we observed marked loss of H3K27me3 near the promoters of both genes and a concurrent increase in the active transcription mark H3K27ac in *STAG2* KO cells (Figures 7G and 7H). Moreover, a prominent STAG2 peak is lost at an upstream enhancer region of *POU3F2* and near the TSS of *NR2F1*, suggesting that in the absence of STAG2, PRC2-mediated suppression of these transcription factors is compromised.

To directly test the functional role of POU3F2 and NR2F1 in the metastatic process, we generated *POU3F2* and *NR2F1* KO cells in the background of clonally selected *STAG2* KO A673 cells (Figures S7G and S7H). Transplantation of *POU3F2* and *NR2F1* KO cells resulted in comparable levels of tumor at the primary site (Figures 7I and 7J). However, *POU3F2* KO, but not *NR2F1* KO, cells displayed reduced infiltration of visceral organs, suggesting that in *STAG2* KO cells the increase in *POU3F2* expression is partially responsible for the enhanced metastatic potential of Ewing sarcoma cells (Figures 7K and 7L).

DISCUSSION

Emerging data demonstrate that cohesin plays a significant role in transcriptional regulation by securing DNA-DNA contacts between enhancers and promoters. By broadly surveying the epigenetic and transcriptional landscape coupled with chromatin interactions, we demonstrate a unique functional role of STAG2 in Ewing sarcoma pathogenesis. Specifically, our studies revealed a critical role for STAG2 in governing the establishment of gene-regulatory architecture underlying oncogenic and developmental programs that undergo reprogramming upon loss of STAG2 to promote disease progression.

While STAG2 and its paralog STAG1 appear to have redundant roles in chromatin cohesion and segregation, STAG2 localized to genomic loci marked by epigenetic modifications associated with enhancers in Ewing sarcoma cells. Importantly, depletion of STAG2 resulted in a compensatory increase in STAG1 protein levels. However, examination of the relative genomic distribution of the increased STAG1 revealed that enhancer-marked regions were insufficiently bound by additional cohesin-SA1. Intriguingly, these enhancer-rich domains were enriched for ETS binding motifs and were also strongly occupied by EWS/FLI1. Consistent with this observation, depletion of STAG2 resulted in reconfiguration of a subset of enhancer-promoter interactions including those associated with EWS/FLI1. Moreover, genes regulated by EWS/FLI1 were among the most enriched for alterations in expression as a consequence of STAG2 loss. While one obvious prediction would be that loss of STAG2 reinforces the EWS/FLI oncogenic program, surprisingly, *STAG2* deletion repressed a subset of EWS/FLI1-regulated genes. In this way, STAG2 loss appears to modulate the expression of a subset of genes directly regulated by EWS/FLI, effectively dampening the activity of the oncogene and promoting an EWS/FLI1 "low" state.

Our data further showed that STAG2 also occupied a subset of PRC2-marked regions, which tend to contain binding motifs for transcription factors involved in neurodevelopmental programs. Notably, these regions were devoid of ETS binding motifs and were poorly occupied by EWS/FLI1, suggesting that cohesin-SA2 may function independently of the EWS/FLI1 oncogenic program to regulate a neurogenic program. Indeed, STAG2 loss altered H3K27me3 levels at the promoters of many genes and also resulted in the deregulation of neurodevelopmental programs.

The exact mechanism by which loss of STAG2 changes the nature of long-range *cis*-chromatin interactions or the regulation of developmental genes by PRC2 is currently unknown. Given the lack of compensation by cohesin-SA1 at enhancer-rich regions, it is tempting to speculate that the absence of a productive cohesin complex at these sites may drive the collapse of enhancer-promoter contacts. However, our data showed that a number of enhancer-promoter interactions in these regions were preserved, and at times were even strengthened in *STAG2* KO cells, arguing against a simple, all-or-none mode of regulation. In addition, at cohesin-SA2- and PRC2-enriched regions, we observed marked deregulation of gene expression

(I) Quantification of bioluminescence signal for whole body. Line graph represents mean ± SEM, n = 8 per group. Two-way ANOVA; ns, not significant.
(J) Bioluminescence images of mice described in (I).
(K) Quantification of bioluminescence signal for upper thoracic cavity after blocking the primary tumor at the lower abdomen. Line graph represents mean ± SEM, n = 8 per group. Two-way ANOVA, ***$p < 0.001$, *$p < 0.05$; ns, not significant.
(L) Bioluminescence images of mice described in (K).
See also Figure S7.

without pervasive changes to *cis*-chromatin interactions. Chromatin interactions are highly dynamic, and a static snapshot garnered from HiChIP is likely to miss a subset of interactions, potentially explaining some of the gaps in our understanding of the underlying process. Additionally, recent findings have revealed that *cis*-chromatin interactions involving polycomb-marked regions may occur at distances bridging several megabases, which may put them outside of the purview of our analysis (Kraft et al., 2020; Rhodes et al., 2020; Zhang et al., 2020). Therefore, additional studies are needed to further delineate the exact molecular mechanism by which loss of STAG2 brings about fundamental changes to transcriptional programs.

At the cellular level, STAG2 loss enhanced the migratory and metastatic potential of Ewing sarcoma cells. These finding are in good agreement with clinical observations that showed strong correlation between loss-of-function *STAG2* mutations alone or in combination with *TP53* loss and the incidence of metastasis in patients with Ewing sarcoma (Crompton et al., 2014; Tirode et al., 2014). Given the pleiotropic consequences of STAG2 loss, the relative contribution of each toward the metastatic phenotype is currently unclear. Recent data demonstrates that titration of EWS/FLI1 transcriptional activity promotes cellular plasticity, which may be necessary for Ewing sarcoma cells facing changes in environmental pressures, such as cells undergoing metastasis (Franzetti et al., 2017). Although we did not find a strong overlap between our own dataset and the proteomics-based characterization by Franzetti and colleagues, likely due to differences in the model systems utilized, each of our findings converge on the idea that an EWS/FLI1 "low" state may enable metastases (Franzetti et al., 2017). On the other hand, there is a growing body of evidence highlighting the role of latent developmental program hijacking in metastatic disease (Gupta et al., 2005; Pomerantz et al., 2020). In our study, we observed a dominant representation of neurodevelopmental programs as the transcriptional fingerprints of STAG2 loss. In addition, the expression of a number of neurodevelopmental transcription factors were altered in the wake of STAG2 depletion, including the neural crest specifiers *FOXD3* and *SOX9*, as well as the master regulator of neural progenitor cell differentiation *POU3F2* (Cheung and Briscoe, 2003; Lukoseviciute et al., 2018). Interestingly, *POU3F2* was one of the most significantly induced genes in *STAG2* KO cells. Moreover, recent studies in melanoma and prostate cancer have revealed a critical role for POU3F2 in driving the metastatic process (Bishop et al., 2017; Fane et al., 2019). Thus, we used POU3F2 as a linchpin to assess the potential contribution of the altered neurodevelopmental programs to the metastatic process in Ewing sarcoma. Importantly, our studies revealed that POU3F2 may indeed contribute to the enhanced metastatic potential observed in *STAG2* KO cells, as its repression partially attenuated their metastatic invasion. Therefore, taken together, our results provide strong direct evidence for the involvement of altered neurogenic programs in driving the metastatic process downstream of STAG2 loss. Furthermore, our results also implicate STAG2 loss-mediated modulation of the EWS/FLI1-dependent oncogenic program as an additional candidate mediator of metastasis in Ewing sarcoma, a finding that warrants validation in future studies. Finally, because the cohesin complex plays several important roles in the cell, other functions not explored in this work, such as its role in DNA damage and repair (Meisenberg et al., 2019; Mondal et al., 2019), RNA processing (Kim et al., 2019), immune signaling (Ding et al., 2018), and telomere maintenance (Daniloski and Smith, 2017), may be altered in the context of *STAG2* mutations, and are topics also worthy of exploration in future studies.

STAR★METHODS

Detailed methods are provided in the online version of this paper and include the following:

- KEY RESOURCES TABLE
- RESOURCE AVAILABILITY
  - Lead contact
  - Materials availability
  - Data and code availability
- EXPERIMENTAL MODELS AND SUBJECT DETAILS
  - Animals
  - Zebrafish
  - Cell lines
- METHOD DETAILS
  - CRISPR/Cas9 genome editing
  - Generation of clonal *STAG2* KO Ewing sarcoma cells
  - Cumulative cell growth
  - Cell viability
  - Analysis of growth in semi-solid methylcellulose media
  - Cell cycle profile analysis by EDU incorporation
  - Sub-cellular protein fractionation
  - Co-immunoprecipitation
  - Chromatin immunoprecipitation-sequencing
  - ChIP-seq library preparation & sequencing
  - HiChIP
  - ATAC-sequencing
  - Genome-wide expression profiling
  - Quantitative PCR
  - Zebrafish model of migration
  - Murine xenograft studies
  - DepMap data analysis
  - Genome scale CRISPR/Cas9 screen
  - RNA-Seq analysis
  - ChIP-seq data analysis
  - ATAC-Seq
  - ChIP-Seq and ATAC-Seq visualization and analysis
  - Defining cohesin clusters
  - Motif enrichment analysis
  - Generation of EWS/FLI1 gene signatures
  - GSEA analysis of transcriptome and proteomic data
  - Enricher and GO analysis
  - HiChIP data analysis
- QUANTIFICATION AND STATISTICAL ANLAYSIS

SUPPLEMENTAL INFORMATION

Supplemental information can be found online at https://doi.org/10.1016/j.ccell.2021.05.007.

ACKNOWLEDGMENTS

This work was funded by the NCI R01 CA204915 (K.S), RO1 supplement 3R01 CA204915-03S1 (B.A), St Jude's Collaborative Research Consortium (K.S),

Curing Kids Cancer (K.S), St. Baldrick's Foundation (B.D.C., N.V.D.), the NCI K08 CA188073 (B.D.C.), Ewing Cancer Foundation of Canada (J.N.B.), and the C[17] Childhood Cancer Canada Foundation (J.N.B.). B.K.A.S. is supported by a Department of Defense PRCRP Horizon Award (CA181249). S.L. is a Leukemia Lymphoma Society fellow. D.L. is supported by TC32GM007753 from NIGMS. We thank Nick Barrowman at the Children's Hospital of Eastern Ontario and Clement Ma at Dana-Farber Cancer Institute for their guidance on statistical analyses.

AUTHOR CONTRIBUTIONS

B.A.: Conceptualization, investigation, analysis, writing, visualization. G.A.: Methodology, investigation, analysis, writing, visualization. E.E.H.: Methodology, investigation, analysis, writing, visualization. D.H.: Methodology, investigation, analysis, writing, visualization. C.A.L.: Methodology, investigation, analysis, writing, visualization. B.K.A.S.: Investigation, analysis, writing, visualization. F.S.D.C.: Investigation, analysis, writing, visualization. M.R.: Investigation, analysis, writing, visualization. A.S.W.: Investigation, analysis, writing, visualization. S.W.: Investigation, analysis, writing, visualization. S.L.: Investigation, analysis, writing, visualization. A.L.R.: Methodology, analysis. A.S.C.: Methodology, analysis. A.B.I.: Investigation, analysis, writing, visualization. N.V.D.: Methodology, investigation, analysis, writing, visualization. D.L.: Investigation, analysis, writing, visualization. B.T.: Investigation, analysis, writing, visualization. J.M.K.-B.: Investigation, analysis, writing, visualization. F.V.: Investigation, analysis, writing, visualization. M.S.: Investigation, analysis, writing, visualization. J.N.B.: Conceptualization, writing, supervision, funding. A.L.K.: Conceptualization, writing, supervision, funding. S.A.C.: Conceptualization, supervision, writing. M.J.A.: Conceptualization, supervision, writing. R.A.Y.: Conceptualization, analysis, writing, funding. B.D.C.: Conceptualization, investigation, analysis, writing, visualization. K.S.: Conceptualization, analysis, writing, funding.

DECLARATION OF INTERESTS

None of the authors declare a conflict of interest for this project but report the following relationships. N.V.D. is a current employee of Genentech, Inc., a member of the Roche Group. R.A.Y. is a founder and shareholder of Syros Pharmaceuticals, Camp4 Therapeutics, Omega Therapeutics, and Dewpoint Therapeutics. M.J.A. has financial interests in Monitor Biotechnologies (formerly known as Beacon Genomics). K.S. receives grant funding as part of the DFCI/Novartis Drug Discovery Program, consults for and has stock options in Auron Therapeutics, and consulted for AstraZeneca and Kronos Bio. B.D.C. receives research funding from Gradalis for an unrelated project, and his spouse was previously employed by Shire and Mersana and currently works for Acceleron.

INCLUSION AND DIVERSITY

One or more of the authors of this manuscript self-identifies as an underrepresented ethnic minority in science, self-identifies as a member of the LGBTQ+ community, and received support from a program designed to increase minority representation in science.

Received: July 16, 2019
Revised: January 28, 2021
Accepted: May 13, 2021
Published: June 14, 2021

REFERENCES

Aguirre, A.J., Meyers, R.M., Weir, B.A., Vazquez, F., Zhang, C.Z., Ben-David, U., Cook, A., Ha, G., Harrington, W.F., Doshi, M.B., et al. (2016). Genomic copy number dictates a gene-independent cell response to CRISPR/Cas9 targeting. Cancer Discov. *6*, 914–929.

Armentano, M., Chou, S.J., Tomassy, G.S., Leingartner, A., O'Leary, D.D., and Studer, M. (2007). COUP-TFI regulates the balance of cortical patterning between frontal/motor and sensory areas. Nat. Neurosci. *10*, 1277–1286.

Armentano, M., Filosa, A., Andolfi, G., and Studer, M. (2006). COUP-TFI is required for the formation of commissural projections in the forebrain by regulating axonal growth. Development *133*, 4151–4162.

Aynaud, M.M., Mirabeau, O., Gruel, N., Grossetete, S., Boeva, V., Durand, S., Surdez, D., Saulnier, O., Zaidi, S., Gribkova, S., et al. (2020). Transcriptional programs define intratumoral heterogeneity of Ewing sarcoma at single-cell resolution. Cell Rep. *30*, 1767–1779 e1766.

Balbas-Martinez, C., Sagrera, A., Carrillo-de-Santa-Pau, E., Earl, J., Marquez, M., Vazquez, M., Lapi, E., Castro-Giner, F., Beltran, S., Bayes, M., et al. (2013). Recurrent inactivation of STAG2 in bladder cancer is not associated with aneuploidy. Nat. Genet. *45*, 1464–1469.

Benedetti, L., Cereda, M., Monteverde, L., Desai, N., and Ciccarelli, F.D. (2017). Synthetic lethal interaction between the tumour suppressor STAG2 and its paralog STAG1. Oncotarget *8*, 37619–37632.

Bishop, J.L., Thaper, D., Vahid, S., Davies, A., Ketola, K., Kuruma, H., Jama, R., Nip, K.M., Angeles, A., Johnson, F., et al. (2017). The master neural transcription factor BRN2 is an androgen receptor-suppressed driver of neuroendocrine differentiation in prostate cancer. Cancer Discov. *7*, 54–71.

Brohl, A.S., Solomon, D.A., Chang, W., Wang, J., Song, Y., Sindiri, S., Patidar, R., Hurd, L., Chen, L., Shern, J.F., et al. (2014). The genomic landscape of the Ewing Sarcoma family of tumors reveals recurrent STAG2 mutation. PLoS Genet. *10*, e1004475.

Buenrostro, J.D., Giresi, P.G., Zaba, L.C., Chang, H.Y., and Greenleaf, W.J. (2013). Transposition of native chromatin for fast and sensitive epigenomic profiling of open chromatin, DNA-binding proteins and nucleosome position. Nat. Methods *10*, 1213–1218.

Carroll, T.S., Liang, Z., Salama, R., Stark, R., and de Santiago, I. (2014). Impact of artifact removal on ChIP quality metrics in ChIP-seq and ChIP-exo data. Front. Genet. *5*, 75.

Cheung, M., and Briscoe, J. (2003). Neural crest development is regulated by the transcription factor Sox9. Development *130*, 5681–5693.

Crompton, B.D., Stewart, C., Taylor-Weiner, A., Alexe, G., Kurek, K.C., Calicchio, M.L., Kiezun, A., Carter, S.L., Shukla, S.A., Mehta, S.S., et al. (2014). The genomic landscape of pediatric Ewing sarcoma. Cancer Discov. *4*, 1326–1341.

Cuadrado, A., Gimenez-Llorente, D., Kojic, A., Rodriguez-Corsino, M., Cuartero, Y., Martin-Serrano, G., Gomez-Lopez, G., Marti-Renom, M.A., and Losada, A. (2019). Specific contributions of cohesin-SA1 and cohesin-SA2 to TADs and polycomb domains in embryonic stem cells. Cell Rep. *27*, 3500–3510.e4.

Daniloski, Z., and Smith, S. (2017). Loss of tumor suppressor STAG2 promotes telomere recombination and extends the replicative lifespan of normal human cells. Cancer Res. *77*, 5530–5542.

Ding, S., Diep, J., Feng, N., Ren, L., Li, B., Ooi, Y.S., Wang, X., Brulois, K.F., Yasukawa, L.L., Li, X., et al. (2018). STAG2 deficiency induces interferon responses via cGAS-STING pathway and restricts virus infection. Nat. Commun. *9*, 1485.

Doench, J.G., Fusi, N., Sullender, M., Hegde, M., Vaimberg, E.W., Donovan, K.F., Smith, I., Tothova, Z., Wilen, C., Orchard, R., et al. (2016). Optimized sgRNA design to maximize activity and minimize off-target effects of CRISPR-Cas9. Nat. Biotechnol. *34*, 184–191.

Dowen, J.M., Fan, Z.P., Hnisz, D., Ren, G., Abraham, B.J., Zhang, L.N., Weintraub, A.S., Schujiers, J., Lee, T.I., Zhao, K., and Young, R.A. (2014). Control of cell identity genes occurs in insulated neighborhoods in mammalian chromosomes. Cell *159*, 374–387.

El-Naggar, A.M., Veinotte, C.J., Cheng, H., Grunewald, T.G., Negri, G.L., Somasekharan, S.P., Corkery, D.P., Tirode, F., Mathers, J., Khan, D., et al. (2015). Translational activation of HIF1alpha by YB-1 promotes sarcoma metastasis. Cancer Cell *27*, 682–697.

Fane, M.E., Chhabra, Y., Smith, A.G., and Sturm, R.A. (2019). BRN2, a POUerful driver of melanoma phenotype switching and metastasis. Pigment Cell Melanoma Res. *32*, 9–24.

Franzetti, G.A., Laud-Duval, K., van der Ent, W., Brisac, A., Irondelle, M., Aubert, S., Dirksen, U., Bouvier, C., de Pinieux, G., Snaar-Jagalska, E., et al.

(2017). Cell-to-cell heterogeneity of EWSR1-FLI1 activity determines proliferation/migration choices in Ewing sarcoma cells. Oncogene *36*, 3505–3514.

Gao, X.L., Zheng, M., Wang, H.F., Dai, L.L., Yu, X.H., Yang, X., Pang, X., Li, L., Zhang, M., Wang, S.S., et al. (2019). NR2F1 contributes to cancer cell dormancy, invasion and metastasis of salivary adenoid cystic carcinoma by activating CXCL12/CXCR4 pathway. BMC Cancer *19*, 743.

Gupta, P.B., Kuperwasser, C., Brunet, J.P., Ramaswamy, S., Kuo, W.L., Gray, J.W., Naber, S.P., and Weinberg, R.A. (2005). The melanocyte differentiation program predisposes to metastasis after neoplastic transformation. Nat. Genet. *37*, 1047–1054.

Haering, C.H., Farcas, A.M., Arumugam, P., Metson, J., and Nasmyth, K. (2008). The cohesin ring concatenates sister DNA molecules. Nature *454*, 297–301.

Haldi, M., Ton, C., Seng, W.L., and McGrath, P. (2006). Human melanoma cells transplanted into zebrafish proliferate, migrate, produce melanin, form masses and stimulate angiogenesis in zebrafish. Angiogenesis *9*, 139–151.

Hansen, A.S., Cattoglio, C., Darzacq, X., and Tjian, R. (2018). Recent evidence that TADs and chromatin loops are dynamic structures. Nucleus *9*, 20–32.

He, T., Surdez, D., Rantala, J.K., Haapa-Paananen, S., Ban, J., Kauer, M., Tomazou, E., Fey, V., Alonso, J., Kovar, H., et al. (2017). High-throughput RNAi screen in Ewing sarcoma cells identifies leucine rich repeats and WD repeat domain containing 1 (LRWD1) as a regulator of EWS-FLI1 driven cell viability. Gene *596*, 137–146.

Heinz, S., Benner, C., Spann, N., Bertolino, E., Lin, Y.C., Laslo, P., Cheng, J.X., Murre, C., Singh, H., and Glass, C.K. (2010). Simple combinations of lineage-determining transcription factors prime cis-regulatory elements required for macrophage and B cell identities. Mol. Cell *38*, 576–589.

Kagey, M.H., Newman, J.J., Bilodeau, S., Zhan, Y., Orlando, D.A., van Berkum, N.L., Ebmeier, C.C., Goossens, J., Rahl, P.B., Levine, S.S., et al. (2010). Mediator and cohesin connect gene expression and chromatin architecture. Nature *467*, 430–435.

Kim, J.S., He, X., Liu, J., Duan, Z., Kim, T., Gerard, J., Kim, B., Pillai, M.M., Lane, W.S., Noble, W.S., et al. (2019). Systematic proteomics of endogenous human cohesin reveals an interaction with diverse splicing factors and RNA-binding proteins required for mitotic progression. J. Biol. Chem. *294*, 8760–8772.

Kojic, A., Cuadrado, A., De Koninck, M., Gimenez-Llorente, D., Rodriguez-Corsino, M., Gomez-Lopez, G., Le Dily, F., Marti-Renom, M.A., and Losada, A. (2018). Distinct roles of cohesin-SA1 and cohesin-SA2 in 3D chromosome organization. Nat. Struct. Mol. Biol. *25*, 496–504.

Kon, A., Shih, L.Y., Minamino, M., Sanada, M., Shiraishi, Y., Nagata, Y., Yoshida, K., Okuno, Y., Bando, M., Nakato, R., et al. (2013). Recurrent mutations in multiple components of the cohesin complex in myeloid neoplasms. Nat. Genet. *45*, 1232–1237.

Kraft, K., Yost, K.E., Murphy, S., Magg, A., Long, Y., Corces, M.R., Granja, J.M., Mundlos, S., Cech, T.R., Boettiger, A., and Chang, H.Y. (2020). Polycomb-mediated genome architecture enables long-range spreading of H3K27 methylation. bioRxiv. https://doi.org/10.1101/2020.07.27.223438.

Lareau, C.A., and Aryee, M.J. (2018). hichipper: a preprocessing pipeline for calling DNA loops from HiChIP data. Nat. Methods *15*, 155–156.

Lareau, C.A., Aryee, M.J., and Berger, B. (2018). diffloop: a computational framework for identifying and analyzing differential DNA loops from sequencing data. Bioinformatics *34*, 672–674.

Lee, L.M., Seftor, E.A., Bonde, G., Cornell, R.A., and Hendrix, M.J. (2005). The fate of human malignant melanoma cells transplanted into zebrafish embryos: assessment of migration and cell division in the absence of tumor formation. Dev. Dyn. *233*, 1560–1570.

Li, H., and Durbin, R. (2010). Fast and accurate long-read alignment with Burrows-Wheeler transform. Bioinformatics *26*, 589–595.

Li, W., Xu, H., Xiao, T., Cong, L., Love, M.I., Zhang, F., Irizarry, R.A., Liu, J.S., Brown, M., and Liu, X.S. (2014). MAGeCK enables robust identification of essential genes from genome-scale CRISPR/Cas9 knockout screens. Genome Biol. *15*, 554.

Liao, Y., Smyth, G.K., and Shi, W. (2014). featureCounts: an efficient general purpose program for assigning sequence reads to genomic features. Bioinformatics *30*, 923–930.

Liu, Y., Xu, H., Van der Jeught, K., Li, Y., Liu, S., Zhang, L., Fang, Y., Zhang, X., Radovich, M., Schneider, B.P., et al. (2018). Somatic mutation of the cohesin complex subunit confers therapeutic vulnerabilities in cancer. J. Clin. Invest. *128*, 2951–2965.

Livak, K.J., and Schmittgen, T.D. (2001). Analysis of relative gene expression data using real-time quantitative PCR and the 2(-Delta Delta C(T)) method. Methods *25*, 402–408.

Losada, A., Yokochi, T., Kobayashi, R., and Hirano, T. (2000). Identification and characterization of SA/Scc3p subunits in the *Xenopus* and human cohesin complexes. J. Cell Biol. *150*, 405–416.

Lukoseviciute, M., Gavriouchkina, D., Williams, R.M., Hochgreb-Hagele, T., Senanayake, U., Chong-Morrison, V., Thongjuea, S., Repapi, E., Mead, A., and Sauka-Spengler, T. (2018). From pioneer to repressor: bimodal foxd3 activity dynamically remodels neural crest regulatory landscape in vivo. Dev. Cell *47*, 608–628.e6.

McLean, C.Y., Bristor, D., Hiller, M., Clarke, S.L., Schaar, B.T., Lowe, C.B., Wenger, A.M., and Bejerano, G. (2010). GREAT improves functional interpretation of cis-regulatory regions. Nat. Biotechnol. *28*, 495–501.

Meisenberg, C., Pinder, S.I., Hopkins, S.R., Wooller, S.K., Benstead-Hume, G., Pearl, F.M.G., Jeggo, P.A., and Downs, J.A. (2019). Repression of transcription at DNA breaks requires cohesin throughout interphase and prevents genome instability. Mol. Cell *73*, 212–223.e7.

Meyers, R.M., Bryan, J.G., McFarland, J.M., Weir, B.A., Sizemore, A.E., Xu, H., Dharia, N.V., Montgomery, P.G., Cowley, G.S., Pantel, S., et al. (2017). Computational correction of copy number effect improves specificity of CRISPR-Cas9 essentiality screens in cancer cells. Nat. Genet. *49*, 1779–1784.

Mondal, G., Stevers, M., Goode, B., Ashworth, A., and Solomon, D.A. (2019). A requirement for STAG2 in replication fork progression creates a targetable synthetic lethality in cohesin-mutant cancers. Nat. Commun. *10*, 1686.

Mumbach, M.R., Rubin, A.J., Flynn, R.A., Dai, C., Khavari, P.A., Greenleaf, W.J., and Chang, H.Y. (2016). HiChIP: efficient and sensitive analysis of protein-directed genome architecture. Nat. Methods *13*, 919–922.

Nasmyth, K. (2002). Segregating sister genomes: the molecular biology of chromosome separation. Science *297*, 559–565.

Ochi, Y., Kon, A., Sakata, T., Nakagawa, M.M., Nakazawa, N., Kakuta, M., Kataoka, K., Koseki, H., Nakayama, M., Morishita, D., et al. (2020). Combined cohesin-RUNX1 deficiency synergistically perturbs chromatin looping and causes myelodysplastic syndromes. Cancer Discov. *10*, 836–853.

Olson, H.M., and Nechiporuk, A.V. (2018). Using zebrafish to study collective cell migration in development and disease. Front. Cell Dev. Biol. *6*, 83.

Phanstiel, D.H., Boyle, A.P., Heidari, N., and Snyder, M.P. (2015). Mango: a bias-correcting ChIA-PET analysis pipeline. Bioinformatics *31*, 3092–3098.

Pohl, A., and Beato, M. (2014). bwtool: a tool for bigWig files. Bioinformatics *30*, 1618–1619.

Pomerantz, M.M., Qiu, X., Zhu, Y., Takeda, D.Y., Pan, W., Baca, S.C., Gusev, A., Korthauer, K.D., Severson, T.M., Ha, G., et al. (2020). Prostate cancer reactivates developmental epigenomic programs during metastatic progression. Nat. Genet. *52*, 790–799.

Postel-Vinay, S., Veron, A.S., Tirode, F., Pierron, G., Reynaud, S., Kovar, H., Oberlin, O., Lapouble, E., Ballet, S., Lucchesi, C., et al. (2012). Common variants near TARDBP and EGR2 are associated with susceptibility to Ewing sarcoma. Nat. Genet. *44*, 323–327.

Quinlan, A.R., and Hall, I.M. (2010). BEDTools: a flexible suite of utilities for comparing genomic features. Bioinformatics *26*, 841–842.

Ramirez, F., Ryan, D.P., Gruning, B., Bhardwaj, V., Kilpert, F., Richter, A.S., Heyne, S., Dundar, F., and Manke, T. (2016). deepTools2: a next generation web server for deep-sequencing data analysis. Nucleic Acids Res. *44*, W160–W165.

Rhodes, J.D.P., Feldmann, A., Hernandez-Rodriguez, B., Diaz, N., Brown, J.M., Fursova, N.A., Blackledge, N.P., Prathapan, P., Dobrinic, P., Huseyin,

M.K., et al. (2020). Cohesin disrupts polycomb-dependent chromosome interactions in embryonic stem cells. Cell Rep. *30*, 820–835.e10.

Riggi, N., Knoechel, B., Gillespie, S.M., Rheinbay, E., Boulay, G., Suva, M.L., Rossetti, N.E., Boonseng, W.E., Oksuz, O., Cook, E.B., et al. (2014). EWS-FLI1 utilizes divergent chromatin remodeling mechanisms to directly activate or repress enhancer elements in Ewing sarcoma. Cancer Cell *26*, 668–681.

Romero-Perez, L., Surdez, D., Brunet, E., Delattre, O., and Grunewald, T.G.P. (2019). STAG mutations in cancer. Trends Cancer *5*, 506–520.

Sankar, S., Theisen, E.R., Bearss, J., Mulvihill, T., Hoffman, L.M., Sorna, V., Beckerle, M.C., Sharma, S., and Lessnick, S.L. (2014). Reversible LSD1 inhibition interferes with global EWS/ETS transcriptional activity and impedes Ewing sarcoma tumor growth. Clin. Cancer Res. *20*, 4584–4597.

Savola, S., Klami, A., Myllykangas, S., Manara, C., Scotlandi, K., Picci, P., Knuutila, S., and Vakkila, J. (2011). High expression of complement component 5 (C5) at tumor site associates with superior survival in Ewing's sarcoma family of tumour patients. ISRN Oncol. *2011*, 168712.

Servant, N., Varoquaux, N., Lajoie, B.R., Viara, E., Chen, C.J., Vert, J.P., Heard, E., Dekker, J., and Barillot, E. (2015). HiC-Pro: an optimized and flexible pipeline for Hi-C data processing. Genome Biol. *16*, 259.

Smith, R., Owen, L.A., Trem, D.J., Wong, J.S., Whangbo, J.S., Golub, T.R., and Lessnick, S.L. (2006). Expression profiling of EWS/FLI identifies NKX2.2 as a critical target gene in Ewing's sarcoma. Cancer Cell *9*, 405–416.

Solomon, D.A., Kim, J.S., Bondaruk, J., Shariat, S.F., Wang, Z.F., Elkahloun, A.G., Ozawa, T., Gerard, J., Zhuang, D., Zhang, S., et al. (2013). Frequent truncating mutations of STAG2 in bladder cancer. Nat. Genet. *45*, 1428–1430.

Solomon, D.A., Kim, T., Diaz-Martinez, L.A., Fair, J., Elkahloun, A.G., Harris, B.T., Toretsky, J.A., Rosenberg, S.A., Shukla, N., Ladanyi, M., et al. (2011). Mutational inactivation of STAG2 causes aneuploidy in human cancer. Science *333*, 1039–1043.

Sosa, M.S., Parikh, F., Maia, A.G., Estrada, Y., Bosch, A., Bragado, P., Ekpin, E., George, A., Zheng, Y., Lam, H.M., et al. (2015). NR2F1 controls tumour cell dormancy via SOX9- and RARbeta-driven quiescence programmes. Nat. Commun. *6*, 6170.

Subramanian, A., Tamayo, P., Mootha, V.K., Mukherjee, S., Ebert, B.L., Gillette, M.A., Paulovich, A., Pomeroy, S.L., Golub, T.R., Lander, E.S., and Mesirov, J.P. (2005). Gene set enrichment analysis: a knowledge-based approach for interpreting genome-wide expression profiles. Proc. Natl. Acad. Sci. U S A *102*, 15545–15550.

Thorvaldsdottir, H., Robinson, J.T., and Mesirov, J.P. (2013). Integrative Genomics Viewer (IGV): high-performance genomics data visualization and exploration. Brief Bioinformatics *14*, 178–192.

Tirode, F., Surdez, D., Ma, X., Parker, M., Le Deley, M.C., Bahrami, A., Zhang, Z., Lapouble, E., Grossetete-Lalami, S., Rusch, M., et al. (2014). Genomic landscape of Ewing sarcoma defines an aggressive subtype with co-association of STAG2 and TP53 mutations. Cancer Discov. *4*, 1342–1353.

Tomazou, E.M., Sheffield, N.C., Schmidl, C., Schuster, M., Schonegger, A., Datlinger, P., Kubicek, S., Bock, C., and Kovar, H. (2015). Epigenome mapping reveals distinct modes of gene regulation and widespread enhancer reprogramming by the oncogenic fusion protein EWS-FLI1. Cell Rep. *10*, 1082–1095.

Tsherniak, A., Vazquez, F., Montgomery, P.G., Weir, B.A., Kryukov, G., Cowley, G.S., Gill, S., Harrington, W.F., Pantel, S., Krill-Burger, J.M., et al. (2017). Defining a cancer dependency map. Cell *170*, 564–576.e16.

Urban, S., Kobi, D., Ennen, M., Langer, D., Le Gras, S., Ye, T., and Davidson, I. (2015). A Brn2-Zic1 axis specifies the neuronal fate of retinoic-acid-treated embryonic stem cells. J. Cell Sci. *128*, 2303–2318.

van der Lelij, P., Lieb, S., Jude, J., Wutz, G., Santos, C.P., Falkenberg, K., Schlattl, A., Ban, J., Schwentner, R., Hoffmann, T., et al. (2017). Synthetic lethality between the cohesin subunits STAG1 and STAG2 in diverse cancer contexts. eLife *6*, e26980.

Varet, H., Brillet-Gueguen, L., Coppee, J.Y., and Dillies, M.A. (2016). SARTools: a DESeq2- and EdgeR-based R pipeline for comprehensive differential analysis of RNA-seq data. PLoS One *11*, e0157022.

Weintraub, A.S., Li, C.H., Zamudio, A.V., Sigova, A.A., Hannett, N.M., Day, D.S., Abraham, B.J., Cohen, M.A., Nabet, B., Buckley, D.L., et al. (2017). YY1 is a structural regulator of enhancer-promoter loops. Cell *171*, 1573–1588.e28.

Westerfield, M. (2000). The zebrafish book. In A guide for the laboratory use of zebrafish (Danio rerio), 4th ed (Eugene: University of Oregon Press).

Wendt, K.S., Yoshida, K., Itoh, T., Bando, M., Koch, B., Schirghuber, E., Tsutsumi, S., Nagae, G., Ishihara, K., Mishiro, T., et al. (2008). Cohesin mediates transcriptional insulation by CCCTC-binding factor. Nature *451*, 796–801.

White, R.M., Sessa, A., Burke, C., Bowman, T., LeBlanc, J., Ceol, C., Bourque, C., Dovey, M., Goessling, W., Burns, C.E., and Zon, L.I. (2008). Transparent adult zebrafish as a tool for in vivo transplantation analysis. Cell Stem Cell *2*, 183–189.

Yao, Z., Mich, J.K., Ku, S., Menon, V., Krostag, A.R., Martinez, R.A., Furchtgott, L., Mulholland, H., Bort, S., Fuqua, M.A., et al. (2017). A single-cell roadmap of lineage bifurcation in human ESC models of embryonic brain development. Cell Stem Cell *20*, 120–134.

Zeng, H., Jorapur, A., Shain, A.H., Lang, U.E., Torres, R., Zhang, Y., McNeal, A.S., Botton, T., Lin, J., Donne, M., et al. (2018). Bi-allelic loss of CDKN2A initiates melanoma invasion via BRN2 activation. Cancer Cell *34*, 56–68.e9.

Zhang, X., Jeong, M., Huang, X., Wang, X.Q., Wang, X., Zhou, W., Shamim, M.S., Gore, H., Himadewi, P., Liu, Y., et al. (2020). Large DNA methylation Nadirs anchor chromatin loops maintaining hematopoietic stem cell identity. Mol. Cell *78*, 506–521.e6.

Zhang, Y., Liu, T., Meyer, C.A., Eeckhoute, J., Johnson, D.S., Bernstein, B.E., Nusbaum, C., Myers, R.M., Brown, M., Li, W., and Liu, X.S. (2008). Model-based analysis of ChIP-seq (MACS). Genome Biol. *9*, R137.

Zhou, C., Qiu, Y., Pereira, F.A., Crair, M.C., Tsai, S.Y., and Tsai, M.J. (1999). The nuclear orphan receptor COUP-TFI is required for differentiation of subplate neurons and guidance of thalamocortical axons. Neuron *24*, 847–859.

Zhu, A., Ibrahim, J.G., and Love, M.I. (2019). Heavy-tailed prior distributions for sequence count data: removing the noise and preserving large differences. Bioinformatics *35*, 2084–2092.

STAR★METHODS

KEY RESOURCES TABLE

REAGENT OR RESOURCE	SOURCE	IDENTIFIER
Antibodies		
Mouse anti-STAG2 (Western blot)	Santa Cruz	Cat#sc-81852; RRID: AB_2199948
Rabbit anti-STAG2 (ChIP-seq)	Cell Signaling	Cat#5882; RRID:AB_10834529
Rabbit anti-STAG1(Western blot)	Bethyl	Cat# A302-579A;RRID:AB_2034857
Rabbit anti-STAG1(ChIP-seq)	Bethyl	Cat# A302-578A; RRID:AB_2034858
Rabbit anti-SMC1A	Bethyl	Cat# A300-055A; RRID:AB_2192467
Rabbit anti-RAD21	Bethyl	Cat# A300-080A; RRID:AB_2176615
Rabbit anti-SMC3	Bethyl	Cat# A300-060A, RRID:AB_67579
Rabbit anti-H3K27me3	Cell Signaling	Cat# 4395, RRID:AB_11220433
Rabbit anti-EWS/FLI1	Abcam	Cat# ab15289; RRID:AB_301825
Rabbit anti -alpha TUBULIN	Cell Signaling	Cat# 2144; RRID:AB_2210548
Mouse anti-GAPDH	Santa Cruz	Cat# sc-47724; RRID:AB_627678
Rabbit anti-H3K27ac3	Abcam	Cat# ab4729, RRID:AB_2118291
Rabbit anti-POU3F2	Cell Signaling	Cat# 12137; RRID:AB_2797827
Rabbit anti-NR2F1	Cell Signaling	Cat# 6364; RRID:AB_11220432
Normal Rabbit IgG-R	Cell Signaling	Cat# 2729; RRID:AB_1031062
Drosophila H2Az(spike-in Antibody)	Active Motif	Cat#61686; RRID: AB_2737370
Rat anti-MouseIgG2a HRP conjugated secondary	GenWay	Cat# 25-783-70745;RRID:AB_1028627
Sheep Anti-Mouse IgG ECL Antibody, HRP Conjugated	GE Healthcare	Cat# NA9310-1ml; RRID:AB_772193
Chemicals, peptides, and recombinant proteins		
Bovine serum albumin	Sigma-Aldrich	Cat#F2442
Phosphate Buffer Saline	DFCI supply center	NA
RPMI medium	DFCI supply center	NA
DMEM medium	DFCI supply center	NA
Penicillin-Streptomycin	Gibco	Cat#15070063
Sodium Pyruvate	ThermoFisher	Cat#21051040
Puromycin	Gibco	Cat#A1113802
Polybrene	American Bio	Cat#AB01643
TransIT-VirusGEN transfection reagent	Mirus	Cat#MIR 6704
X-tremeGENE™ HP DNA Transfection Reagent	Sigma	Cat#6366236001
ClonaCell-TCS medium	Stem Cells	Cat#03814
MTT labeling reagent	Sigma	Cat#11 465 007 001
Trypan Blue	Gibco	Cat#15250061
Cell Titer -Glo	Promega	Cat#G7570
4′,6-diamidino-2-phenylindole (DAPI)	Sigma	Cat#D9542
Pierce IP Lysis Buffer	Thermofisher	Cat#87788
16% methanol-free Formaldehyde solution (w/v)	Thermofisher	Cat#28908
5M NaCl	Thermofisher	Cat#AM9760G
Tris-EDTA pH 8.0	Sigma-Aldrich	Cat#93283
Ultrapure 0.5M EDTA	Invitrogen	Cat#15575-038
Ultrapure 1M Tris-HCl pH 8.0	Invitrogen	Cat#15568-025
Ultrapure 10% SDS	Invitrogen	Cat#15553-035
2.5M Glycine solution	BostonBioProducts	Cat#C-4375
Halt protease inhibitors	Thermofisher	Cat#78429
phenylmethylsulfonyl fluoride (PMSF)	Sigma-Aldrich	Cat#P7626

(*Continued on next page*)

Continued

REAGENT OR RESOURCE	SOURCE	IDENTIFIER
Transposase,TAGMENT DNA Enzyme	Illumina	Cat#15027865
Dynabeads Protein A	Invitrogen	Cat#10004D
Lithium Chloride	Sigma	Cat#L9650
NP40	Fisher	Cat#FNN021
Deoxycholic acid	Fisher	Cat#BP349-100
NaHCO3	Sigma	Cat#S5761
NaN3	USB	Cat#21610
Triton X-100	Sigma	Cat#0992-93-1
Igepal CA-630	Sigma	Cat#I8896
Agencourt AMPure XP	Beckman Coulter	Cat#A63881
Critical commercial assays		
qScript cDNA synthesis Kit	QuantaBio	Cat#95047-025
SYBR Green FastMix	QuantaBio	Cat#95072-250
Click-iT™ Plus EdU Flow Cytometry Assay Kit	Thermofisher	Cat#C10634
Subcellular Protein Fractionation Kit	Thermofisher	Cat#87787
Deposited data		
ChIP-Seq, RNA-Seq, ATAC-Seq, Hi-ChIP	This study	GEO:GSE116495
Ewing sarcoma Proteome	This study	http://massive.ucsd.eduMSV000082954
Ewing sarcoma RNA-Seq	(Crompton et al., 2014)	dbGaP: phs000804.v1.p1
Ewing sarcoma ChIP-Seq	(Riggi et al., 2014)	GEO: GSE61953
Ewing sarcoma ChIP-Seq, RNA-seq	(Tomazou et al., 2015)	http://tomazou2015.computational-epigenetics.org
Ewing sarcoma ChIP-Seq	(Kojic et al., 2018)	GEO: GSE101921
Ewing sarcoma ChIP-Seq	ENCODE: ENCSR000DZP	GEO: GSM935376
Ewing sarcoma Affymetrix arrays	(Postel-Vinay et al., 2012)	GEO: GSE34620
Ewing sarcoma Affymetrix arrays	(Savola et al., 2011)	GEO: GSE17618
Ewing sarcoma RNA-Seq	(Smith et al., 2006)	GEO: GSE53066
Ewing sarcoma RNA-Seq	(Sankar et al., 2014)	NCBI: PRJNA176544
Ewing sarcoma Affymetrix arrays	(Smith et al., 2006)	Array Express: E-GEOD-4560
Ewing sarcoma RNA-Seq	(He et al., 2017)	GEO: GSE73092
Ewing sarcoma IC-EwS gene signature	(Aynaud et al., 2020)	https://www.sciencedirect.com/science/article/pii/S2211124720300747?via=ihub
Experimental models: organisms/strains		
Mouse: NOD.Cg-Prkdcscid Il2rgtm1Wjl/SzJ (NSG)	The Jackson Laboratory	Cat# JAX:005557;RRID:IMSR_JAX:005557
Zebrafish: *Tg(nacre$^{-/-}$; roy$^{-/-}$)*(*Caspers*)	Dr. Leonard Zon Lab, DFCI	NA
Experimental models: cell lines		
Human: A673 (Female)	Dr. Todd Golub Lab, Broad Institute	NA
Human: TC71 (Male)	Dr. Todd Golub Lab, Broad Institute	NA
Human: TC32 (Female)	Dr. Todd Golub Lab, Broad Institute	NA
Human: EW8 (Male)	Dr. Todd Golub Lab, Broad Institute	NA
Human: SKPNDW (Male)	DR. Alejandro Sweet-Cordero Lab, Stanford University	NA
Oligonucleotides		
sgSTAG2#1 gRNA AATGTCTTACTGCTCTACAA	IDT	NA
sgSTAG2#4 gRNA GCTGAATGTCATCCTCCCGT	IDT	NA
sgSTAG1#2 gRNA GGAATTAGAGGAGCAGGCCG	IDT	NA
sgSTAG2#3 gRNA CAGCGAGCTTGAAGAAACAG	IDT	NA
sgNT1 gRNA GTAGCGAACGTGTCCGGCGT	IDT	NA
sgNT2 gRNA GACCGGAACGATCTCGCGTA	IDT	NA

(*Continued on next page*)

Continued

REAGENT OR RESOURCE	SOURCE	IDENTIFIER
sgPOU3F2-A gRNA GCTGTAGTGGTTAGACGCTG	IDT	NA
sgNR2F1-A gRNA GTACTGGCCTGGATTGGGCT	IDT	NA
sgLACZ gRNA AACGGCGGATTGACCGTAAT	IDT	NA
Recombinant DNA		
pVSVg (addGene 8454)	Addgene	RRID:Addgene_8454
pPAX2 (addGene 19319)	Addgene	RRID:Addgene_1226
lentiCRISPR v2	Addgene	RRID:Addgene_52961
pSpCas9BB-2A-GFP(PX458)	Addgene	RRID:Addgene_48138
CMV-GFP-T2A-Luciferase plasmid	SBI	Cat#BLIV101PA-1
Software and algorithms		
Prism 8	Graphpad	http://www.graphpad.com
FlowJo V9.9.6	Tree Star	http://www.flowjo.com/
ImageQuant TL 8.2	Cytiva	https://www.cytivalifesciences.com

RESOURCE AVAILABILITY

Lead contact

Further information and requests for resources and reagents should be directed to and will be fulfilled by the Lead Contact, Kimberly Stegmaier (Kimberly.stegmaier@dfci.harvard.edu).

Materials availability

This study did not generate new unique reagents. Any additional material or reagent described in this manuscript will be made available with a simple MTA.

Data and code availability

The data from this study including all ChIP-Seq, RNA-Seq, ATAC-Seq and HiChIP was uploaded at GEO under the accession number GSE116495. The proteomics data from this study is available at the following link http://massive.ucsd.eduMSV000082954. Ewing sarcoma tumor RNA-Seq data previously reported by (Crompton et al., 2014) is available at dbGaP with the following accession number dbGaP: phs000804.v1.p1. Ewing sarcoma ChIP-Seq previously reported by (Riggi et al., 2014) is available at GEO with the following accession number GEO: GSE61953. Ewing sarcoma ChIP-Seq and RNA-seq data previously reported by (Tomazou et al., 2015) is available at the following link http://tomazou2015.computational-epigenetics.org. Ewing sarcoma ChIP-Seq data previously reported by (Kojic et al., 2018) is available at GEO with the following accession number GEO: GSE101921. Ewing sarcoma ChIP-Seq data previously reported at ENCODE: ENCSR000DZP is available at GEO under the accession number GEO: GSM935376. Ewing sarcoma tumor Affymetrix arrays data previously reported by (Postel-Vinay et al., 2012) available at GEO with the following accession number GEO: GSE34620. Ewing sarcoma tumor Affymetrix arrays data previously reported by (Savola et al., 2011) is available at GEO with the following accession number GEO: GSE17618. Ewing sarcoma RNA-Seq data previously reported by (Smith et al., 2006) is available at GEO with the following accession number GEO: GSE53066. Ewing sarcoma RNA-Seq data previously reported by (Sankar et al., 2014) is available at NCBI with the following accession number NCBI: PRJNA176544. Ewing sarcoma Affymetrix arrays data previously reported by (Smith et al., 2006) is available at Array express with the following accession number Array Express: E-GEOD-4560. Ewing sarcoma RNA-Seq data previously reported by (He et al., 2017) is available at GEO with the following accession number GEO: GSE73092. Ewing sarcoma IC-EwS gene signature previously reported by (Aynaud et al., 2020) is available at the following link https://www.sciencedirect.com/science/article/pii/S2211124720300747?via=ihub.

EXPERIMENTAL MODELS AND SUBJECT DETAILS

Animals

All mice were housed at Dana-Farber Cancer institute's animal facility. All mouse procedures were conducted in accordance with the Guidelines for the Care and Use of Laboratory Animals and were approved by the Institutional Animal Care and Use Committee at Dana-Farber Cancer Institute. For all experiments, female 6-8 weeks old NOD.Cg-Prkdcscid Il2rgtm1Wjl/SzJ (NSG) mice were obtained from Jackson laboratory and allowed to acclimatize for one week prior to transplantation. The details of individual xenograft studies including the method of transplantation, the cell dose used, and nature of data acquisition is described in the methods details section.

Zebrafish

Zebrafish (*Danio rerio*) were raised and maintained according to standard protocol (Westerfield, 2000). *Tg(nacre*$^{-/-}$*; roy*$^{-/-}$*)* zebrafish, commonly called caspers, were used for all *in vivo* experiments (White et al., 2008). Adult fish were maintained in a recirculating commercial housing system at 28.5℃ under a 14:10 light: dark condition schedule. The optimal temperature for zebrafish growth occurs at 28°C; however, to accommodate the injected cancer cell lines, zebrafish larvae used in xenotransplantation (XT) experiments were incubated at 35°C to allow for normal growth and development of both zebrafish and injected human cell lines (Haldi et al., 2006; Lee et al., 2005). All zebrafish larvae were maintained in E3 embryo medium (5 mM NaCl, 0.17 mM KCl, 0.33 mM $CaCl_2$, 0.33 mM $MgSO_4$) in 10 cm petri dishes. Larvae were cleaned and provided with new media daily. Larvae were euthanized by tricaine overdose (1 mg/ml) at seven days post fertilization (dpf), followed by 6.15% bleach solution to ensure complete mortality. Use of zebrafish in this study was approved by the Dalhousie University Committee on Laboratory Animals (protocol # 17-005).

Cell lines

All cell lines used in this study were previously genotyped and confirmed to express the appropriate EWS-ETS rearrangement using either a combination of whole-exome sequencing and transcriptome sequencing or a combination of STR profiling and RT-PCR (Crompton et al., 2014). A673 (female), EW8 (male), and SKPNDW (male) cells were grown in Dulbecco's modified Eagle's media (Mediatech) with 10% FBS (Sigma-Aldrich) and 1% penicillin streptomycin glutamine (Gibco). A673 medium was supplemented with 1 mmol/L sodium pyruvate (Gibco). TC71 (male) and TC32 (female) cells were grown in RPMI (Mediatech) with 10% FBS and 1% penicillin streptomycin glutamine (Gibco). A673, TC71, TC32 and EW8 were provided by Dr. Todd Golub (Broad Institute, Cambridge, MA) and SKPNDW by Dr. Alejandro Sweet-Cordero (Stanford University, Stanford, CA).

METHOD DETAILS

CRISPR/Cas9 genome editing

LentiCRISPRv2 plasmid backbone encoding Cas9 nuclease and a puromycin resistance gene was digested with the restriction endonuclease BsmbI, gel extracted and used in a ligation reaction with synthetic oligonucleotide fragments for guide RNA sequences (gRNA) targeting a gene of interest. Oligos were purchased from Integrated DNA Technologies (IDT), annealed and end phosphorylated via T4 polynucleotide kinase before using in the ligation reaction. All gRNA sequences used in this manuscript are provided in the key resources table under the oligonucleotide heading. Lentiviral particles were generated by co-transfecting cells with 2 μgs of lentiCRISPRv2-gRNA constructs along with viral packaging plasmids pVSVg (Addgene 8454) and pPAX2 (Addgene 19319) into HEK293T cells using TransIT-VirusGEN transfection reagent (Mirus). Ewing sarcoma cells plated 2-3 days prior were transduced with fresh viral particles, cultured for 48 hours and subjected to puromycin selection at 1 μg/ml for 72 additional hours. Gene KO was confirmed by immunoblotting for the respective targets.

Generation of clonal *STAG2* KO Ewing sarcoma cells

For TC71 cells, the protocol outlined above was used with the exception of the use of X-tremeGENE™ HP DNA Transfection Reagent (Roche). Puromycin selected cells were seeded in semi-solid methylcellulose-based medium (ClonaCell-TCS Medium, Stemcell Technologies) at clonal density and individual colonies were picked, expanded in liquid culture and gene editing was confirmed by western blotting for STAG2. For A673 cells, pSpCas9BB-2A-GFP(PX458) (Addgene#48138) expressing Cas9 nuclease and EGFP plasmid were used to clone gRNA sequences targeting *STAG2*. A673 cells were transiently transfected with 10 μg of pSpCas9BB-2A-GFP-gRNA using X-tremeGENE™ HP DNA Transfection Reagent. Seventy-two hours later, GFP+ cells were FACS sorted, allowed to expand in liquid culture and re-seeded in ClonaCell-TCS Medium (Stemcell Technologies) at clonal density. Single colonies were picked and expanded in culture and eventually validated for deletion of STAG2 by western blots.

Cumulative cell growth

Parental, non-targeting controls, and *STAG2* KO TC71 and A673 cells were plated in replicates at equal low densities and grown for 3 to 4 days. Live cell counts were assessed by trypan blue exclusion staining and cells were re-plated at the same original density. This was repeated every 3 to 4 days for approximately 2 weeks. At each interval, cell counts were used to determine the number of cell doublings using the formula LOG((x/y),2), where x=total cells per flask, and y=total number of cells seeded per flask. Cell doublings per interval were added to produce a cumulative cell doubling value.

Cell viability

To determine the effects of *STAG1* deletion on cell viability in *STAG2* mutant or *STAG2* depleted Ewing sarcoma cells, cells were plated in 384-well plates at a concentration of 1000 cells per well in 50 μL of medium. Cell viability was measured by adding 10 μL of CellTiter-Glo ATP-based assay (Promega). Luminescence was read using the FLUOstar Omega microplate reader (BMG LabTech).

Analysis of growth in semi-solid methylcellulose media

Parental, non-targeting control and *STAG2* KO TC71 cells were plated in semi-solid methylcellulose-based medium (ClonaCell-TCS Medium, Stemcell Technologies) at a density of 2500 cells/ml in 6 well plates. Fourteen days later, wells containing colonies

propagated in culture were stained with 700 μl of a 1:1 mixture of PBS and MTT labeling reagent (Roche) by incubating for 60 minutes in an incubator at 37°C, >95% humidity and 5% carbon dioxide. Plates were imaged using ImageQuant LAS 4000 imager (GE healthcare) and pictures of individual wells were taken. Colony number in each well and volume per individual colony were determined from the images using the ImageQuant TL 8.2 image analysis software (Cytiva).

Cell cycle profile analysis by EDU incorporation

For cell cycle profile analysis, the Click-iT™ Plus EdU Alexa Fluor™ 647 Flow Cytometry Assay Kit (ThermoFisher Scientific) was used. Log phase growing non-targeting control and *STAG2* KO A673 cells were pulsed with 10 μM of the modified nucleotide analogue EdU (5-ethynyl-2' -deoxyuridine) for 90 minutes in an incubator at 37°C, >95% humidity and 5% carbon dioxide. Cells were harvested, washed, fixed, permeabilized and treated with a reaction cocktail containing Alexa flour 647 conjugated picolyl azide to label incorporated EdU. Cells were treated with RNase for 15 minutes, stained with 4′,6-diamidino-2-phenylindole (DAPI) and subsequently analyzed by flow cytometry.

Sub-cellular protein fractionation

Cells were grown to 80% confluence and a total of five million cells were harvested. The subcellular Protein Fractionation Kit for Cultured Cells (ThermoFisher Scientific) was used to isolate proteins in the soluble cytoplasmic fraction, nuclear soluble fraction and chromatin-bound fraction according to the manufacturer's protocol. Harvested cells were treated with a plasma membrane permeabilization reagent to release soluble cytoplasmic proteins followed by treatment with a reagent to dissolve plasma, mitochondrial and ER/Golgi membranes while maintaining nuclear membrane integrity. Intact nuclei were isolated by centrifugation and their protein content was extracted. Chromatin bound nuclear proteins were released by treating with micrococcal nuclease for 15 minutes at room temperature.

Co-immunoprecipitation

Cells were grown to 80% confluence and a total of five million cells were harvested, washed with ice cold phosphate buffer saline (PBS) and lysed with lysis buffer (pH 7.4, 0.025M Tris, 0.15M NaCl, 0.001M EDTA, 1% NP40, 5% glycerol) supplemented with protease inhibitor cocktail. Five μgs of antibodies were conjugated with 25 μl of magnetic beads. Protein lysates were quantified and resuspended at a concentration of 1 mg/ml in lysis buffer. 250 μls of lysates (per IP) were incubated with the antibody coupled magnetic beads for two hours at room temperature with gentle rotation, washed and eluted to release target antigens.

Chromatin immunoprecipitation-sequencing

Cells (20 million per ChIP reaction for all but EWS/FLI1, which required 40 million cells) were crosslinked with warm 1% methanol-free formaldehyde (ThermoFisher) for 10 minutes at room temperature rotating at 12 RPM. The reaction was quenched by adding glycine to a final concentration of 0.125M and incubating for an additional 5 minutes at room temperature rotating at 12 RPM. Cell pellets were washed three times with ice cold PBS and resuspended in 1 ml of SDS lysis buffer (1% SDS, 10 mM EDTA, 50 mM Tris-HCl pH8) supplemented with protease inhibitor cocktail including phenylmethylsulfonyl fluoride (PMSF) and incubated at RT for 2 minutes with gentle rotation. Lysates were centrifuged at 15,000 G for 10 minutes at 4°C and the pellet was re-suspended in 900 μl of ChIP IP buffer (2:1 SDS lysis buffer : triton dilution buffer), transferred to milliTUBE (Covaris). Sonication was performed on a E220 Focus Ultra Sonicator (Covaris) using the setting (duty cycle 5%, peak power 140W, cycles per burst 200, Temperature 4°C, time 30 minutes/millitube). ChIP inputs from sheared chromatin were de-crosslinked by adding de-crosslinking buffer (NaHCO3, NaCl, RNase A, Proteinase K) and incubating for two hours at 65°C in a thermal cycler. The remaining sheared chromatin was incubated with primary antibody coupled to Protein A DynaBead (Beckman Coulter, antibody bead conjugation was performed for 16 hours) overnight, rotating at 4°C. As a calibration control, antibody against a drosophila specific histone variant H2Av and drosophila chromatin (Active Motif) were used as per the recommendation of the manufacturer. The next day, ChIP product was eluted from the Dynabeads in 100 μl of elusion buffer and de-crosslinked for 12 hours at 65°C. For both Input and chipped material, AMPure XP beads (Beckman coulter) were used to purify DNA. Information regarding antibodies used is presented in key resources table under the heading of Antibodies.

ChIP-seq library preparation & sequencing

ChIP-Seq libraries were prepared using Swift S2 Acel reagents on a Beckman Coulter Biomek i7 liquid handling platform from approximately 1 ng of DNA according to the manufacturer's protocol and 14 cycles of PCR amplification. Finished sequencing libraries were quantified by a Qubit fluorometer and samples were QC'D using a Bioanalyzer Tapestation (Agilent Technologies 2200) to determine fragment size. Library pooling and indexing were evaluated with shallow sequencing on an Illumina MiSeq. Subsequently, libraries were sequenced on a NovaSeq targeting 40 million 100bp read pairs by the Molecular Biology Core facilities at Dana-Farber Cancer Institute.

HiChIP

HiChIP was performed on the A673 clonal lines sgNT-1c4 and sgSTAG2-1c6 in duplicate based on a previously published protocol (Mumbach et al., 2016) with a few adaptations which were performed as previously described (Weintraub et al., 2017). The A673 clonal lines sgNT-1c4 and sgSTAG2-1c6 were tested with duplicates for each line crosslinked on separate occasions. The

SMC1A antibody used in the ChIP experiments was by Bethyl A300-055A. Libraries were sequenced 100x100 on an Illumina Hi-Seq 2500 platform.

ATAC-sequencing

ATAC-Seq was performed on A673 clones (sgNT-1c4, sgNT-2c3, sgSTAG2-1c6, and sgSTAG2-4c5). (Buenrostro et al., 2013) Cells were collected, and apoptotic cells removed with the Annexin V MicroBead Kit (Miltenyi Biotec) according to the manufacturer's protocol. To prepare nuclei, we spun 50,000 cells at 500 × g for 5 minutes. Cells were lysed using cold lysis buffer (10 mM Tris-Cl, pH 7.4, 10 mM NaCl, 3 mM MgCl2 and 0.1% IGEPAL CA-630). Immediately after lysis, nuclei were spun at 500 × g for 10 minutes using a refrigerated centrifuge. Immediately following the nuclei prep, the pellet was resuspended in the transposase reaction mix (25 μL 2x TD buffer, 2.5 μL Transposase (Illumina) and 22.5 μL of nuclease free water). The transposition reaction was carried out for 30 minutes at 37 °C. Directly following transposition the sample was purified using a Qiagen Minelute kit. Transposed DNA was eluted in 10 μL Elution Buffer (10mM Tris buffer, pH 8). We then performed size selection to target fragments of 115-600 bp by Pippin Prep according to manufacturer's instructions. Next, we amplified 20 μL of library fragments after adding 25 μL of NEBnext PCR master mix and 2.5 μL of custom Nextera PCR primers 1 and 2. PCR was performed using the following conditions: 72°C for 5 minutes, 98°C for 30 seconds, followed by thermocycling at 98°C for 10 seconds, 63°C for 30 seconds and 72°C for 1 minute for 12 cycles. We then performed a SPRI PCR cleanup (AMPure XP Beads; Beckman Coulter/Agencourt) and confirmed that the final library fragments were 100-800 bp by Tapestation.

Genome-wide expression profiling

Total RNA was extracted with an RNeasy Kit (Qiagen) from *STAG2* wild-type and *STAG2* knockout clones (A673.sgNT-1c4, A673.sgNT-2c3, A673.sgLacZ-2c1, A673.sgSTAG2-1c4, A673.sgSTAG2-1c6, A673.sgSTAG2-4c3, A673.sgSTAG2-4c5, TC71.sgNT-1c6, TC71.sgNT-2c5, TC71.sgSTAG2-1c6, TC71.sgSTAG2-4c15, TC71.sgSTAG2-4c18, TC71.sgSTAG2-1c3). For the A673 clones, Poly(A) RNA was isolated using the NEBNext mRNA magnetic isolated module (New England Biolabs) and paired-end libraries were prepared using the NEBNext Ultra Directional RNA Library Prep Kit for Illumina (New England Biolabs) according to the manufacturer's protocols with the following modifications: the PCR library enrichment conditions were adjusted to 12 cycles and the PCR library reaction was purified twice by size selection with Agencourt AMPure XP beads (Beckman Coulter). Libraries were subjected to 50 base paired-end sequencing (Illumina HiSeq 2000). For the TC71 clones, Total RNA was extracted with the RNeasy Kit and on-column DNA digestion (Qiagen). Poly(A) mRNA was isolated, and libraries were prepared using the TruSeq Stranded mRNA Kit (Illumina) according to the manufacturer's protocol. Strand-specific mRNA sequencing libraries were pooled and sequenced on a NextSeq500 instrument with single-end 75bp reads to a depth of 30-40M reads/sample.

Quantitative PCR

RNA was extracted from cells using the RNeasy Mini kit and on-column DNA digestion (Qiagen) and quantified using Qubit RNA HS Assay (ThermoFisher Scientific). cDNA was prepared using qScript cDNA synthesis Kit (QuantaBio) and a C1000 Touch Thermal Cycler (Bio-Rad). Data were collected in technical triplicates and biological duplicate using SYBR Green FastMix (QuantaBio) on QuantStudio™ 6 -Flex Real-Time PCR Systems (Life Technologies) and analyzed using the ΔΔCT method (Livak and Schmittgen, 2001).

Zebrafish model of migration

Fluorescently labeled TC71 cells clonally selected for *STAG2* KO (sgSTAG2-1c6, sgSTAG2-4c15, and sgSTAG2-4c18) or WT *STAG2* expression (sgNT-1c6 and sgNT-2c5) were injected into the hindbrain ventricle (HBV) of zebrafish larvae 2 days post-fertilization (dpf). The needle tip was positioned perpendicular to the otolith of the zebrafish larvae and inserted directly into the HBV for the transplantation of 50-100 cells. After injection, zebrafish were monitored with brightfield and fluorescent microscopy and scored for presence of migrated TC71 cells to the dorsal surface, yolk sac and tail. To demonstrate that migration does not occur passively, larvae with fluorescent microspheres (~10 microns) were also injected into the HBV at 2 dpf. Larvae were monitored to confirm that there was no microsphere migration into the dorsal surface, yolk sac and tail. Each TC71 clone was injected into a minimum of 120 zebrafish. For analysis, all *STAG2* KO clones were combined (n = 403) and all WT *STAG2* clones were combined (n = 433). The percentage of fish in the *STAG2* KO group and Control group were calculated and a 95% confidence interval was estimated with the modified Wilson method. Fisher's exact test was used to determine whether a difference in the rate of migration was significant at day 3 post-injection, the day where the maximum migration rate was reached in this experiment.

Murine xenograft studies

Two tail vein injection mouse xenograft experiments were conducted to test the effect of *STAG2* knockout on metastasis. In the first experiment, A673 cells clonally selected for *STAG2* KO or WT *STAG2* expression (sgNT-1c4, sgNT-2c3, sgSTAG2-1c4, sgSTAG2-1c6, sgSTAG2-4c5, and sgSTAG2-4c5) were transduced with the lentiviral plasmid pFUW-Luc-Neo to constitutively express luciferase. One million cells were injected into the tail vein of each NSG mouse such that 6 mice were injected with each clone. Mice were then monitored for the presence of metastasis by serial bioluminescence imaging. For analysis, data from mice injected with *STAG2* KO clones were combined and mice with WT *STAG2* clones were combined. The two groups were compared by mixed-effects model with multiple comparisons. One mouse treated with sgSTAG2-4c5 clones died from disease prior to day 30.

In the second experiment, TC71 cells were transduced with the lentiviral plasmid encoding GFP-T2A-Luciferase and selected by fluorescence-activating cell sorting (FACS) for GFP expression. Cells were then transduced with lentiviral CRISPR Cas9 *STAG2*-targeting guides (sgSTAG2-1 and sgSTAG2-4) or a non-targeting guide (sgNT-1). Cells were selected for transduction by puromycin for five days and knockout of *STAG2* was confirmed by western immunoblot before 500,000 cells of each condition were injected into the tail vein of NSG mice. Mice were then monitored for the presence of metastasis by serial bioluminescence imaging with the abdomen blocked to measure metastatic sites (lower extremities) distant from the initial target organs of the injection (liver and lungs). Five mice were injected with each sgSTAG2 treated condition and 10 mice were injected with sgNT-1 treated cells. One mouse injected with sgNT-1 and one mouse injected with sgSTAG2-4 treated cells died shortly after tail vein injection and was excluded from bioluminescence analysis. For analysis, data from mice injected with *STAG2* KO clones were combined. The two groups were compared by mixed-effects model with multiple comparisons.

A third semi-orthotopic intramuscular injection mouse xenograft experiment was conducted to test the effect of *STAG2* knockout on metastasis. Clonally selected A673 cells (NT1c4, sgSTAG2#1-c6, sgSTAG2#4-c5) were transduced with the lentiviral plasmid encoding GFP-T2A-Luciferase and selected by fluorescence-activating cell sorting (FACS) for GFP expression. Cells were washed and resuspended in 1:1 mixture of Matrigel/PBS and injected directly into the hind limb cranial thigh muscle away from sciatic nerve at a concentration of 50,000 cells per mouse in 50 μl Matrigel solution. We used 8 NSG mice per group and monitored for disease progression and the presence of metastasis by serial bioluminescence imaging of whole body as well as the upper thoracic cavity after blocking the primary tumor site. At the conclusion of the experiment, lungs from all recipient mice were extracted and BLI imaging was performed *ex vivo* tissue culture plates.

In a separate experiment, TC32 cells were transduced with the lentiviral plasmid encoding GFP-T2A-Luciferase and selected by fluorescence-activating cell sorting (FACS) for GFP expression. Cells were then transduced with lentiviral CRISPR Cas9 *TP53*-targeting guides (sgTP53-1 and sgTP53-5) or a non-targeting guide (sgNT-1). These polyclonal cells were selected for transduction by puromycin for five days and knockout of *TP53* was confirmed by western immunoblot before 250,000 cells of each condition were injected into the tail vein of NSG mice (n=5 per group). Mice were then monitored for overall disease progression and the presence of metastasis by serial bioluminescence imaging of whole body and with the abdomen blocked to measure metastatic colonization of the lower extremities.

To assess the effect of *POU3F2* and *NR2F1* on the metastatic potential of *STAG2* KO cells, we used one of the clonally selected *STAG2* KO cells (sgSTAG2#1-c6) and transduced it with the lentiviral plasmid encoding GFP-T2A-Luciferase and selected by fluorescence-activating cell sorting (FACS) for GFP expression. Next, we transduced these cells with lentiviral CRISPR Cas9 targeting guides against (sgPOU3F2-A, sgNR2F1-A or LACZ). Successfully transduced cells were selected with 1 μg/ml of puromycin for 3 days and knockout of each gene validated by western blot. Cells were injected via the intramuscular route as described above at a concentration of 50,000 cells per mouse (n=8 per group) and disease progression was monitored by serial bioluminescence imaging as described above.

DepMap data analysis

CERES Gene effect scores for cohesin genes *STAG2, RAD21, SMC1A* and *SMC3* were downloaded from the CRISPR (Avana) Public Depmap v20Q3 portal https://depmap.org/portal/download/ for the 16 Ewing sarcoma and 773 other lineage cell lines in the database. A lower CERES score indicates a higher likelihood that the gene is essential for the cell line. A CERES score of 0 indicates not essentiality, while a score of -1 is comparable with the median of all pan-essential genes, i.e., the genes which are essential for every cell line. A CERES score below -0.5 is estimated as indicative of gene essentiality for the cell line, while a score above 0.5 is estimated as indicative of tumor suppressor effect. For each cohesin gene, the essentiality effect on Ewing sarcoma cells vs. all other cell lines as background, was visualized on hockey stick plots.

Genome scale CRISPR/Cas9 screen

The genome-scale CRISPR-Cas9 screening was performed using the Broad Institute's Avana library. The isogenic A673 cell lines with either *STAG2* knockout or non-targeting controls were screened with the Avana library, containing 73,372 guides and an average of 4 guides per gene.(Doench et al., 2016; Meyers et al., 2017) The screens were conducted in a pooled experiment as previously described.(Aguirre et al., 2016; Meyers et al., 2017).

The isogenic A673 cell lines with either *STAG2* knockout or non-targeting controls were screened in replicate (n=4) with the Avana CRISPR library after pooled transduction into a population of cells. The essential genes in the isogenic lines were identified using MAGeCK.(Li et al., 2014) The Avana guides were filtered to include guides that only map to one location in the genome as MAGeCK does not model the cutting effect of guides that map to multiple locations in the reference genome. Next, the guides were filtered to only include guides that had predicted efficacy scores of >0.95 as modeled by CERES on a large collection of cancer cell lines in order to minimize off-target effects.(Meyers et al., 2017) Thus, the maximum-likelihood analysis of gene essentialities function from MAGeCK was run with 4 replicates of each isogenic line (A673.sgSTAG2-1c6, A673.sgSTAG2-4c5, A673.sgNT-1c4, A673.sgNT-2c3) and approximately 41,978 guides mapping to 17,146 genes. The MAGeCK maximum-likelihood analysis assigned a gene essentiality score for each isogenic line collapsing the replicates.

RNA-Seq analysis

The human reads were mapped to the GRCh37/hg19 human genome using STAR v2.7.3 with standard parameters --outSAMtype BAM SortedByCoordinate --outSAMunmapped Within --outSAMattributes NH HI NM MD AS XS --outReadsUnmapped Fastx --outSAMstrandField intronMotif --quantMode TranscriptomeSAM GeneCounts --quantTranscriptomeBan IndelSoftclipSingleend. Quality control for the mapped reads and for replicate reproducibility was performed using SARTools v1.7.3 (Varet et al., 2016). Gene level reads were summarized by counting the reads that overlapped the GRCh37/hg19 annotated gene exons, by using the featureCounts v1.6.3 method implemented in the Subread v2.0.0 package (http://subread.sourceforge.net) (Liao et al., 2014). Gene counts were normalized and used to quantify differential genes between the experimental and control conditions using DESeq2 v1.24.0. Genes with $\geq$10 reads across at least 3 samples (A673 data) and across at least 2 samples (TC71 data) were annotated as "expressed". Differentiability for the expressed genes was assessed with DESeq2 based on the robust shrunken log2 fold change scores and the approximate posterior estimation for GLM coefficients (apeglm v1.6, Zhu et al., (2019)) method for effect size. The cutoffs for differentially expressed genes were $|\log2(\text{fold change})| \geq 1.5$ and adjusted P-value ≤ 0.10. Heatmap for transcriptional data visualization was created by using the Morpheus software platform (https://software.broadinstitute.org/morpheus/) based on the log2(1+ DESeq2 normalized counts) data. The RNA-Seq data for this study are available for download from the Gene Expression Omnibus (GEO) repository (GSE 116495).

ChIP-seq data analysis

Quality control tests for unmapped sequences were performed based on the FastQC v.0.11.5 software (http://www.bioinformatics.babraham.ac.uk/projects/fastqc/). All of the ChIP-Seq data sets were aligned to the GRCh37/hg19 human genes and *Drosophila Melanogaster* dm6 genes using bowtie2-2.3.5 with the standard options. PCR duplicates were removed with the Picard v2.18.2 MarkDuplicates tool (Li and Durbin, 2010). The Active Motif Spike-in Normalization protocol was then applied to each hg19 sample by multiplying the human tag counts with the normalization factors derived from the uniquely mapped Drosophila reads as ratios between the sample with the lowest dm6 counts vs. the dm6 counts for that sample.

For each mark the reads mapped on the *STAG2* wild-type clones A673.sgNT-1c4 and A673.sgNT-2c3 were merged and labeled as "*STAG2* WT". Similarly, for each mark the reads mapped on the *STAG2* knockout clones A673.sgSTAG2-1c6, A673.sgSTAG2-4c5 were merged and labeled as "*STAG2* KO" with the exception of H3K27me3 for which only the A673.sgSTAG2-1c6 clone is available and labeled as "*STAG2* KO".

The dm6 normalization factors for individual clones and for the merged clones were very close to 1. The mapped reads for individual and for merged clones were normalized in units of Reads Per Kilobase per Million (RPKM or rpm/bp) and coverage tracks for the RPKM signal were created as bigwig files for bins of size 20 base pairs by using the bamCoverage tool available in deepTools v2.5.3. (Ramirez et al., 2016).

Peak calling was performed against input controls using the model-based MACS2 v2.1.1.20160309 software (Zhang et al., 2008), with the cut-off FDR $\leq$ 0.01. Narrow peaks were identified for all marks except H3K27me3 for which MACS2 was called with the *broad peak* option. Area under Curve (AUC) RPKM normalized signal across genomic regions was computed with the bwtool software (Pohl and Beato, 2014). Peaks with low area under curve coverage (< 300 RPKM) were disregarded and the ENCODE blacklisted regions for hg19 (available at https://www.encodeproject.org/annotations/ENCSR636HFF/) were removed from each set of peak regions. Quality control tests for the mapped reads were performed by using the ChIPQC library available from Bioconductor v3.6 (Carroll et al., 2014). The distances between replicates for *STAG2* WT and *STAG2* KO clones were estimated based on the multiBamSummary function available from the deepTools v2.5.3. (Ramirez et al., 2016) and visualized on correlation heatmaps and PCA plots. The peaks were annotated with the closest hg19 genes by using the annotatePeaks function available in the Homer v4.11 package (Heinz et al., 2010) and the GREAT annotation platform (McLean et al., 2010).

ATAC-Seq

ATAC-Seq data were collected using paired-end 50 bp reads from HiSeq, Illumina at the Center for Cancer Genome Discovery at the Dana-Farber Cancer Institute (2015). Quality control tests for unmapped reads were performed based on the FastQC v.0.11.5 software (Babraham Bioinformatics, http://www.bioinformatics.babraham.ac.uk/projects/fastqc/). All of the ATAC-Seq data sets were aligned to the GRCh37/hg19 human genes using bwa v0.7.17 (https://github.com/lh3/bwa) with the mem -M options (Li and Durbin, 2010). The mitochondrial reads (chr M) were removed with samtools after alignment. PCR duplicates were removed with Picard v2.18.2 MarkDuplicates tool. The reads mapped on the *STAG2* wild-type clones were merged and labeled "*STAG2* WT", and similarly, the reads mapped on the *STAG2* knockout clones were merged and labeled "*STAG2* KO". The mapped reads were normalized in units of Reads Per Kilobase per Million (RPKM or rpm/bp) and coverage tracks for the RPKM signal were created as bigwig files for bins of size 20 base pairs by using the bamCoverage tool available in deepTools v2.5.3 (Ramirez et al., 2016). Model-based peaks were identified using model-based MACS2 v2.1.1.20160309 software (Zhang et al., 2008), with the cut-off FDR $\leq$ 0.01. The ATAC-Seq data for this study is available for download from the Gene Expression Omnibus (GEO) repository (GSE 116495).

ChIP-Seq and ATAC-Seq visualization and analysis

ChIP-Seq binding peaks and normalized binding signal were visualized on the Integrative Genomic Viewer (IGV) v2.4.0 platform. (Thorvaldsdottir et al., 2013) Gene promoter regions were defined as the +/- 3 kb intervals around the hg19 gene transcription start site (TSS). Enhancer regions were required to exist outside of the promoter regions defined as +/- 3 kb from a TSS. The BEDTools

v2.27 (Quinlan and Hall, 2010) was used to perform various genomic region analyses (sorting, intersection, merging). Heatmaps of AUC ChIP-Seq normalized signal occupancy on genomic regions were created using the computeMatrix and the plotHeatmap tools available in the deepTools v2.5.3 suite. The plotProfile tool from deepTools v2.5.3 was used to create metaplots based on the average normalized scores across genomic regions. Differential genome-wide mark binding in *STAG2* KO vs. *STAG2* WT clones was quantified based on the unpaired t-test with Welch correction (cutoff P-value $\leq$ 0.05) for the area under curve (AUC) RPKM normalized signal across the genome-wide regions in the two conditions. For a specific genomic region, the *STAG2* KO vs. *STAG2* WT changes in signal occupancy were classified as ''increase'', ''decrease'' or ''not significant'' based on the absolute cut-off 1.5 for the delta area under curve scores.

Defining cohesin clusters

SA2 binding peak regions not overlapping with SA1 peaks were labeled ''SA2-only''. Overlapping peak regions for both SA1 and SA2 were labeled ''Common''. SA2-only regions bound by H3K27me3 broad peaks were labeled ''SA2/H3K27me3''. SA2-only regions bound by H3K27ac peaks (promoter or enhancer sites) were labeled ''SA2/H3K27ac-Promoters'' and ''SA2/H3K27ac-Enhancers'', respectively. SA2-only regions without H3K27me3 or H3K27ac overlapping peaks were labeled ''SA2/others''.

Motif enrichment analysis

The motif enrichment analysis was performed for genomic regions and gene promoters using HOMER v4.11 platform (Heinz et al., 2010) with the significance cutoff $P < 0.01$. For motif discovery in input genomic regions, HOMER v4.11 used a background control of 100,000 random sequences that matched the GC-content of the queried input sequences. The random sequences were selected from HOMER's own pre-built internal repository of the collection of human (hg19) sequences of predefined lengths (8,10,12,..) that were extracted from the TSS (+/-50 kb) regions. HOMER removes the bias introduced by lower-order oligo sequences through an additional auto-normalization step, by correcting any imbalances between the input target regions and background sequences in 1-mers, 2-mers and 3-mers. This auto-normalization procedure attempts to remove some of the sequence bias associated with certain genomic regions and the noise that may have been introduced by experimental sequencing.

Generation of EWS/FLI1 gene signatures

A compendium of 33 gene sets: 15 EWS/FLI1 gene signatures in A673 cells and 18 EWS/FLI1 signatures in various other contexts was created based on the following resources:

- The A673 IC-EwS on single cell transcriptomics data (Aynaud et al., 2020).
- Five A673 shEWS/FLI1 transcriptomic signatures: RNA-Seq Lessnick-Pais (2016) GSE53066, Lessnick-Sarkar(2012) PRJNA176544, Tomazou(2015) RNA-Seq http://www.medical-epigenomics.org/papers/tomazou2015, Delattre-Kovar(2017) GSE73092) and Affymetrix Lessnick-Smith(2006) E-GEOD-4560. Each of the RNA-Seq data sets was processed separately based on the RNA-Seq pipeline employed for our study, and the Affy expression data was analyzed by using the limma eBayes package with standard cutoffs ($|\log2(\text{fold change})| \geq 1.5$, adjusted $P \leq 0.1$).
- Consensus A673 RNA of 590 EWS/FLI1 activated, respectively 1,392 repressed gene signatures, based on the rule ''3 out of 5'' A673 shEWS/FLI1 transcriptomic signatures.
- A DNA A673 consensus EWS/FLI1 gene target signature based on the gene targets for the EWS/FLI1 bound regions in our ''high coverage'' A673 EWS/FLI1 ChIP-Seq data which overlap with A673 FLI1 peaks identified in two external studies (Riggi et al., 2014; Tomazou et al., 2015).
- Consensus A673 RNA/DNA EWS/FLI1 of 325 activated and 537 repressed by intersecting the Consensus A673 RNA and Consensus A673 ChIP-Seq EWS/FLI1 gene targets.
- the collection of 16 EWS/FLI1 and Ewing sarcoma signatures in various contexts (not A673 cells) available from the MSigDB v7.1 c2 database.
- two core MSigDB Ewing sarcoma Hancock-Lessnick (2008) signatures.

GSEA analysis of transcriptome and proteomic data

GSEA v4.1 software (Subramanian et al., 2005) was used to identify functional associations of the molecular phenotypes induced by STAG2 loss with the compendia of EWS/FLI1 activated and repressed signatures on A673 cells merged with the MSigDB v7.1 collection c2 of curated pathways and experimental gene sets.

The molecular phenotypes induced by *STAG2* KO vs. *STAG2* wild-type were measured by (i) RNA-Seq expression of the A673 and TC71 cells, (ii) proteome mass spectrometry of A673 cells, (iii) RNA-Seq expression of Ewing sarcoma tumors with loss-of -function mutations in *STAG2* compared to tumors expressing wild type *STAG2*.(Crompton et al., 2014) (iv) RNA-Seq expression of Ewing sarcoma tumors with low *STAG2* expression vs. high *STAG2* expression identified in $\sim$ top 12% tumors in two transcriptome data sets with no information about *STAG2* mutation status: (Savola et al., 2011) GSE17679, 42 Ewing sarcoma tumors, and Postel-Vinay (2012) GSE34620, 117 Ewing sarcoma tumors.

For each of these datasets, the hg19 genes were ranked based on the expression fold change in *STAG2* KO (low) vs. *STAG2* wild type (high) phenotypes. The goal of GSEA was to identify the gene sets that are distributed at the top or at the bottom of the ranked list

of genes based on the Kolmogorov-Smirnov enrichment test. Gene sets with absolute Normalized Enrichment Score $\geq$1.3, a nominal P $\leq$ 0.05 and an FDR $\leq$ 0.25 for the Kolmogorov-Smirnov test were considered significant hits. The results were visualized on volcano plots for the Normalized Enrichment Score (NES) vs. -log10(P) and on GSEA plots.

Enricher and GO analysis

Overlapping enrichment analysis for the genes with significantly altered expression induced by *STAG2* KO in A673 cells (|log2(fold change)| $\geq$1.5, adjusted P < 0.10), was performed against the MSigDB v7.1 collections c2 (canonical pathways and experimental gene sets) and c5 (Gene Ontology). Significant enrichments were quantified based on hypergeometric test (P-value $\leq$0.05, FDR $\leq$0.05) and size overlap $\geq$10.

HiChIP data analysis

HiChIP raw reads were aligned to hg19 human reference genome using HiC-Pro v2.10 (Servant et al., 2015). Each of the four replicate samples was sequenced to a depth > 150M reads. Moreover, each sample passed stringent quality control with a minimum of 23% of all reads mapping to intrachromosomal loci. High-confidence loop calls were inferred using hichipper (Lareau and Aryee, 2018) using the merged union of 368,178 SMC1A ChIP-Seq peaks from both the WT and *STAG2* KO cell lines in our study into 144,863 genomic regions. Long range interactions spanning two anchor regions, termed DNA loops, were derived from linked paired-end reads that overlapped restriction fragments containing this consensus peak of possible loop anchors. In total, 1,836,186 interactions spanning pairs of 102,398 genomic loci were observed among the four samples. As a majority of these interactions represent background proximity ligation, we performed stringent filtering to identify putative biologically functional DNA loops.

We called a set of 56,219 loops naive to any additional genetic or epigenetic annotation that met stringent criteria. These loops contained at least four reads with paired-end tags (PETs) in two or more replicates and were statistically-significant at a distance-dependent P-value of 1% and FDR of 1% based on the per-loop measures from the loop proximity bias correction algorithm originally implemented in Mango (Phanstiel et al., 2015). The set of 56,219 stringently filtered loops served as a basis for differential loop calling between the wild-type and *STAG2* KO mutant cell lines. To identify loops with significant changes in contact coverage (either decrease or increase) in A673 with *STAG2* KO compared to *STAG2* WT cells, differential loops were called at using the *diffloop* (Lareau et al., 2018) package with the cutoffs |abs(fold change contact coverage)| $\geq$2 and P-value $\leq$0.05. Loop edges were annotated for their overlap with gene promoter regions and with ChIP-Seq binding sites for H3K27ac enhancers and EWS/FLI1. Loop were annotated for TSS+/-5kb promoter region landing for hg19 genes, and separately for expressed hg19 genes, in accordance with the 5kb resolution of our HiChIP data.

Enhancer-Promoter loops were defined as the significant loops connecting a H3K27ac enhancer binding site on one anchor and a landing gene promoter (TSS+/-5kb region) on the opposite anchor. Enhancers were identified in the H3K27ac A673 ChIP-Seq data in this study as the H3K27ac binding sites outside the TSS+/-3kb regions. Loop anchors were fully annotated with the hosted enhancer binding sites and gene targets (Table S1).

EWS/FLI1 status was assigned to the significant loops that host a EWS/FLI1 binding site (ChIP-Seq peak) on one anchor and a gene promoter (TSS+/-5kb) region on the opposite anchor. Thus, an EWS/FLI1 loop intermediates the "long interactions" between any of the EWS/FLI1 binding sites on one anchor to any of the gene promoter regions on the opposite anchor.

For the purpose of the EWS/FLI1 loop annotation, we defined a consensus of 11,519 ChIP-Seq EWS/FLI1 binding sites on A673 cells by intersecting the peaks identified in the A673 EWS/FLI1 ChIP-Seq high coverage data in this study (MACS2, FDR $\leq$0.01) with the union of the EWS/FLI1 peaks identified in two published A673 EWS/FLI1 ChIP-Seq studies (Riggi et al., 2014; Tomazou et al., 2015). Based on the consensus EWS/FLI1 peaks we identified 8,957 EWS/FLI1 loops. The anchors of the EWS/FLI1 loops were annotated with the EWS/FLI1 ChIP-Seq binding sites and gene promoter landing regions and with the *STAG2* KO vs. WT differential status information for the host loop and for the gene. The fully annotated collection of all 23,580 EWS/FLI1 binding site – promoter long interactions harbored by the 8,957 EWS/FLI1 loops is available (Table S6) as a resource for exploratory data analyses. The median loop length was examined for association with the differential loop status (increase or decrease) induced by *STAG2* KO for all loops, and separately for enhancer-promoter and EWS/FLI1 loops (unpaired t-test with Welch correction, P-value $\leq$0.10).

QUANTIFICATION AND STATISTICAL ANLAYSIS

Data are expressed as mean ± SEM or mean ± SD as indicated in the figure legends. Group size was determined on the basis of the results of preliminary experiments and no statistical method was used to predetermine sample size. The indicated sample size (n) represents biological replicates. Group allocation and outcome assessment were not performed in a blinded manner. All samples that met proper experimental conditions were included in the analysis. Details of statistical analysis used to determine significance are presented in the respective figure legends.